AD-A094 401 AIR FORCE INST OF TECH WRIGHT-PATTERSON AFB OH SCHOO--ETC F/G 20/13
INVESTIGATION OF LASER HEATING IN COMPONENTS WITH SHARP EDGES.(U)
DEC 80 J F BERKE

UNCLASSIFIED AFIT/GEO/PH/80-3 NL

1 OF 2
AD A094401

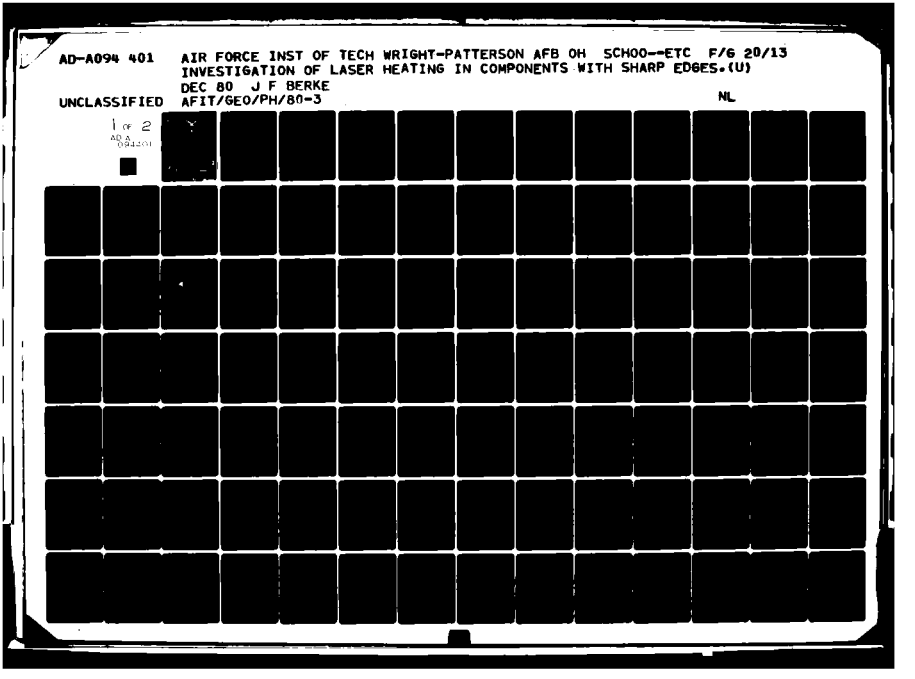

LEVEL II

DEPARTMENT OF THE AIR FORCE
AIR UNIVERSITY (ATC)

AIR FORCE INSTITUTE OF TECHNOLOGY

Wright-Patterson Air Force Base, Ohio

AFIT/GEO/PH/80-3

INVESTIGATION OF LASER HEATING IN COMPONENTS WITH SHARP EDGES

THESIS

AFIT/GEO/PH/80-#3 James F. Berke
2LT USAF

AFIT/GEO/PH/80-3

INVESTIGATION OF LASER HEATING IN COMPONENTS WITH SHARP EDGES

THESIS

Presented to the Faculty of the School of Engineering
of the Air Force Institute of Technology
Air University
in Partial Fulfillment of the
Requirements for the Degree of
Master of Science

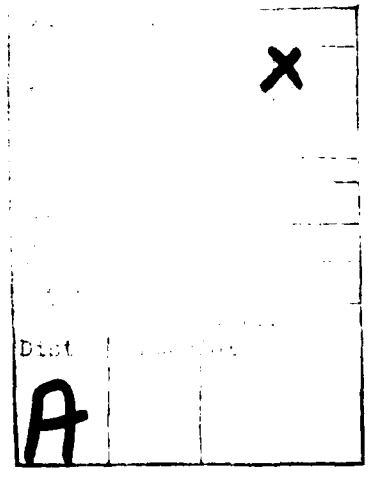

by
James F. Berke, B.S.E.E.
2LT USAF
Graduate Electro-Optics

December 1980

Approved for public release; distribution unlimited.

Preface

This thesis, which investigates sharp edge effects of good conductors illuminated by electromagnetic radiation, has provided me with a tremendous learning experience. I am in greatest debt to my thesis advisor, Major Glenn Doughty, whose patience and guidance kept me going through the worst of times. Most of all, however, was the enthusiasm generated in me by Major Doughty's own enthusiasm for learning.

I would also like to express my gratitude to Les Whitford, who introduced me to the Bessel function subroutine used in this thesis. I would also like to thank Lt Col William F. Bailey and Major Michael R. Stamm, both members of my thesis committee, for their helpful comments. My special thanks goes to my wonderful typist, Sharon A. Gabriel.

Last, but not least, I am truly grateful to my girlfriend, Judy, whose patience and understanding was the key to the completion of this effort.

Table of Contents

List of Figures

List of Figures (Cont'd)

Table of Contents (Cont'd)

List of Tables

Abstract

Numerical results are presented for the approximate time-averaged power density dissipated on the surface of a highly conductive infinite wedge (of angle 90°) near the vicinity of the sharp edge. The numerical results are normalized so one may readily obtain results for varying incident wave frequencies. The angle of incidence of the incident radiation, θ_i (measured with respect to the surface normal of the wedge), is varied from $\theta_i = 0°$ (normal incidence) to $\theta_i = 90°$ (grazing incidence). In particular, numerical results for TE and TM polarization are presented for incident wavelengths of $3.8\mu m$ and $10.6\mu m$. It is assumed that the power density absorbed (watt/m^2) is all converted to heat density.

To accept the validity of the results, an extensive check is made on an arbitrary (real) order Bessel function subroutine used in the equation necessary for the numerical calculations. General electromagnetic theory is also discussed and extended to the use in specific geometries. The geometries considered besides the wedge (though with no numerical results) are the parabolic cylinder and infinite cone.

In conclusion, the numerical results seem very promising due to the success of verifying the Bessel function subroutine used in the calculations.

INVESTIGATION OF LASER HEATING IN COMPONENTS WITH SHARP EDGES

I. Introduction

The number of lasers being used has rapidly increased in the past few years due in a large part to the advent of more sophisticated laser systems and the discovery of new laser applications. The improvement in quality of optical components in lasers has also increased. As a result, the cost of many of the high quality optical components has risen.

Of particular interest to the Air Force Weapons Laboratory (AFWL) at Kirtland Air Force Base, New Mexico, is the investigation of the power dissipated per unit area on the surfaces of highly conductive dielectrics in the vicinity of sharp edges when illuminated by high intensity radiation. The sharp edges arise from the use of rectangular mirrors (having sharp edges) and of cone-shaped mirrors used as waxicons and reflaxicons (see Figures 3 and 4 in Chapter II). Of special interest to AFWL is optical components having a conductivity near that of copper. The incident radiation of interest is in the micron wavelength range (3.8μm and 10.6μm, to be exact). It is feared that the damage threshold of these

optical components may be surpassed near the vicinity of the sharp edges due to induced surface currents, thus having the potential of damaging expensive optical components.

The main objective of this thesis is to calculate the time-averaged power density dissipated on the surface of a highly conductive 90° wedge imbedded in free space. It is assumed that the power density dissipated represents the heat density (in watts per square meter) produced in the wedge from the incident field. The power density is found by first assuming the wedge to be a perfect conductor and finding the surface current density induced on the wedge surface. An approximation is then made to find the power density using the skin depth for a highly conductive linear medium and the surface current density from the perfect conductor case. As such, the power density calculated represents only a first approximation. Numerical calculations, which are believed to be the first made for the geometry and conditions mentioned above, are presented.

In addition to the wedge, two other geometries considered are the cone (representing waxicons) and the parabolic cylinder (representing a flat surface with a rounded edge). Numerical computations using the computer are difficult to obtain for these two geometries, therefore, only the background theory is presented.

This thesis consists of six chapters and four appendices. The chapter immediately following this introduction presents the basic theory necessary to solve the wave equation for the three geometries specified in the following chapter, Chapter III. Chapter IV establishes criteria to verify computer routines to obtain the numerical results for the wedge presented in Chapter V. The final chapter presents the conclusions that can be drawn from Chapter V and recommendations for further study in this area. The four appendices are in support of the thesis.

II. General Background Theory

The purpose of this chapter is to present the general theory necessary to solve the wave equations for the specific geometries discussed in the next chapter. This is accomplished by first presenting Maxwell's equations describing the electric and magnetic fields ($\vec{E}$ and $\vec{H}$) for all space and time. The geometry is that of a perfect electric conductor imbedded in free space and excited by a monochromatic, time-harmonic electromagnetic wave. Once $\vec{E}$ and $\vec{H}$ have been found, the boundary conditions are used to find the induced surface current density ($\vec{J}_s$) . Finally, an approximation to determine the time-averaged power density dissipated on the surface of a good conductor is derived.

Maxwell's Equations and Boundary Conditions

In reference to Figure 1, the following are the assumptions to be made: (1) Region I is assumed to be free space with a conductivity σ = 0 mhos/meter , a permittivity $\epsilon_o = 8.854 \times 10^{-12}$ farad/meter, and a permeability $\mu_o = 4\pi \times 10^{-7}$ henry/meter; (2) Region II is assumed to be a perfect electric conductor with conductivity $\sigma = \infty$, a permittivity μ , and a permeability ϵ ; (3) the source is assumed to be an infinite distance away from

Region II and emitting a monochromatic, time-harmonic electromagnetic (E-M) wave. The E-M wave is assumed to have $e^{i\omega t}$ time dependence, where ω is the radian frequency (in radians/second) of the E-M wave. If the incident electric field $\vec{E}^i$ (where the superscript i represents incident) is polarized such that no component of $\vec{E}^i$ is tangential to the conductor surface, then the incident E-M is said to be transverse magnetic (TM). If the incident magnetic field $\vec{H}^i$ is polarized such that no component of $\vec{H}^i$ is tangential to the conductor surface, then the incident E-M wave is said to be transverse electric (TE). The TM case is considered in the derivations to follow, unless stated otherwise.

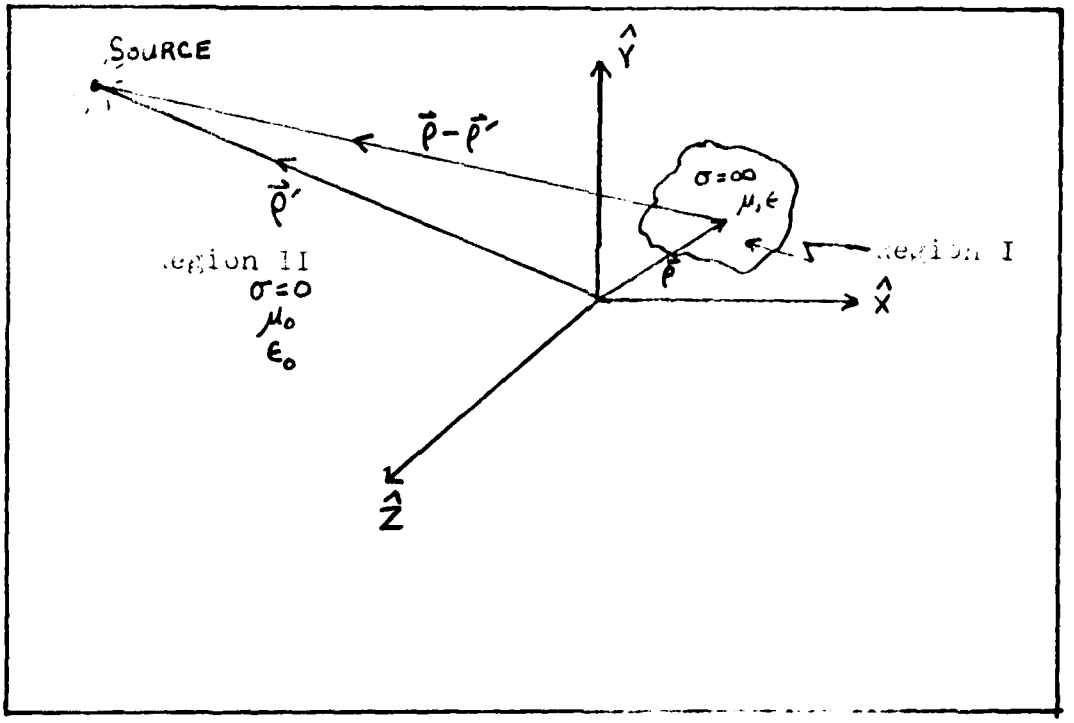

Fig. 1. Perfect Conductor Illuminated By E-M Source

Maxwell's equations for free space near the vicinity of the conductor (hence, neglecting the infinitely distant source) may be written in terms of $\vec{E}$ and $\vec{H}$ as (Ref 1:37,38)

$$\nabla \times \vec{H} = \epsilon_o \frac{\partial \vec{E}}{\partial t} \tag{1}$$

$$\nabla \times \vec{E} = -\mu_o \frac{\partial \vec{H}}{\partial t} \tag{2}$$

$$\nabla \cdot \vec{E} = 0 \tag{3}$$

$$\nabla \cdot \vec{H} = 0 \tag{4}$$

Since $\vec{E}$ and $\vec{H}$ have $e^{i\omega t}$ time dependence and assuming that $\vec{E}$ and $\vec{H}$ can each be expressed as the product of two functions such that one function is a function of space only and the other is a function of time only, then $\frac{\partial \vec{H}}{\partial t} = i\omega\vec{E}$ and $\frac{\partial \vec{E}}{\partial t} = i\omega\vec{H}$. By also using the relation for free space only (Ref 1:38)

$$k = \omega\sqrt{\epsilon_o \mu_o} = \frac{2\pi}{\lambda} \tag{5}$$

where k is known as the propagation constant, $\sqrt{\epsilon_o \mu_o}$ is the inverse of the velocity of E-M waves in free space, and λ is the wavelength of the E-M wave in free space, then Eqs (1) and (2) may be rewritten as

$$\nabla \times \vec{H} = ik\sqrt{\frac{\epsilon_o}{\mu_o}}\,\vec{E} \tag{1'}$$

$$\nabla \times \vec{E} = -ik\sqrt{\frac{\epsilon_o}{\mu_o}}\,\vec{H} \tag{2'}$$

By taking the curl of Eq (2') and substituting Eq (1') for $\nabla \times \vec{H}$ in terms of $\vec{E}$, then

$$\nabla \times \nabla \times \vec{E} - k^2\vec{E} = 0 \tag{6}$$

is obtained. Using the vecotr identity (Ref 1:38)

$$\nabla \times \nabla \times \vec{A} = \nabla(\nabla \cdot \vec{A}) - \nabla^2\vec{A}$$

and recalling that $\nabla \cdot \vec{E} = 0$ from Eq (3), then Eq (6) becomes

$$\nabla^2\vec{E} + k^2\vec{E} = 0 \tag{7}$$

where ∇^2 is the Laplacian operator. In a similar fashion, starting with Eq (1') leads to an equation the same as Eq (7), except with $\vec{E}$ replaced by $\vec{H}$. Equation (7) is the complex vector wave equation that must be solved in order to determine $\vec{E}$. Once $\vec{E}$ is found, the substitution of $\vec{E}$ into Eq (2') determines $\vec{H}$. This gives $\vec{E}$ and $\vec{H}$ for Region I. Since Region II is a perfect conductor,

$\vec{E} = \vec{H} = \vec{J} = 0$ in Region II, where $\vec{J}$ represents the current density (Ref 3:17).

To solve Eq (7) for all space, the boundary conditions for the surface separating Region I from Region II must be given. The boundary conditions, referring to Figure 1, which must be imposed on the surface of the conductor are (Ref 1:34)

$$\hat{n} \times \vec{H} = \vec{J}_s \tag{8}$$

$$\hat{n} \times \vec{E} = 0 \tag{9}$$

where $\hat{n}$ denotes the unit vector normal to the conductor surface and pointing into Region I, and $\vec{J}_s$ denotes the surface current density induced on the conductor surface by the $\vec{H}$ field.

Examination of Eq (9) shows that for any $\hat{n}$, $\hat{n} \times \vec{E} = 0$. Thus, $\vec{E}$ must be equal to zero except when $\vec{E}$ is normal to the surface, in which case $\hat{n} \times \vec{E}$ would necessarily be zero. Thus, there is no tangential component of $\vec{E}$ on the conductor surface. For $\vec{J}_s$ not equal to zero, Eq (8) implies that components of $\vec{H}$ normal to the conductor surface are zero, but the tangential component of $\vec{H}$ on the conductor surface induces a surface current density normal to both $\hat{n}$ and $\vec{H}$.

Recalling that $\vec{E}$ and $\vec{H}$ are separable functions of space and time, Eq (7) can be expressed as a differential equation of only spatial coordinates, since the time dependence will cancel out. For example, if $\vec{E} = \vec{E}_1(u,v,w)f(t)$ where $\vec{E}_1(u,v,w)$ is a vector dependent on spatial coordinates u, v, and w, and $f(t)$ is a scalar function of time t only, then Eq (7) becomes

$$f(t)\,\nabla^2\vec{E}_1(u,v,w) + f(t)k^2\vec{E}_1(u,v,w) = 0$$

For $f(t) \neq 0$, the above equation becomes

$$\nabla^2\vec{E}_1(u,v,w) + k^2\vec{E}_1(u,v,w) = 0 \qquad (10)$$

Equation (10) has the form of a homogeneous, linear partial differential equation of order two. It is also assumed that u, v, and w are independent coordinates of a general three-dimensional orthogonal coordinate system and $E_1(u,v,w)$ is such that

$$E_1(u,v,w) = E_a(u)E_b(v)E_c(w) \qquad (11)$$

where $E_1(u,v,w)$ is the scalar function of $\vec{E}_1(u,v,w)$ and $E_a(u)$, $E_b(v)$, and $E_c(w)$ are separate scalar functions of only one variable. Substitution of Eq (11) into Eq (10) then results in being able to express one side of the equation

depending on only one variable, and the other side of the equation depending on the other two variables. Thus, both sides of the equation must be equal to a constant for any u , v , and w . The process is repeated until three separate ordinary differential equations are obtained for $E_a(u)$, $E_b(v)$, and $E_c(w)$. Solving the differential equations for $E_a(u)$, $E_v(v)$, and $E_c(w)$ and superposition of the solutions in Eq (11) into Eq (10) yields the general solution to $E_1(u,v,w)$.

The method just described is called the method of Separation of Variables (Ref 2:260). The coordinate systems for the specific geometries discussed in the next chapter are such that Eq (7) can be solved by the method of Separation of Variables.

Finite Conductivity Approximations and Scattering

As stated in the Introduction, the main objective of this thesis is to find an approixmation to the time-averaged power density dissipated on the surface of a wedge of high conductivity. This is accomplished by using a parameter known as the skin depth and the surface current density produced on the surface of a perfect conductor as in Eq (8). Because of these two approximations, the following derivations presented for the time-averaged power density loss is just a first approximation to the actual value.

In reference to Figure 1, it is now assumed that the conductor of Region II has a finite conductivity, σ. It is further assumed that Region II is a good conductor, i.e., $\sigma \gg \omega\epsilon$. As stated in the Introduction, the incident radiation of interest is in the micron wavelength (10^{-6} meters) range, hence ω will be on the order of 10^{14} radians per second. The permittivity ϵ of a good conductor is hard to measure, but is generally taken to be on the order of ϵ_o for free space (Ref 1:6). Thus, for copper of $\sigma = 5.8 \times 10^7$ mhos per meter, the condition $\sigma \gg \omega\epsilon$ is well satisfied. It is also assumed that the conductor is a linear isotropic medium.

For good conductors, the surface field amplitude is attenuated by a factor of e^{-1} (0.368) after it has penetrated a distance

$$\delta = \left(\frac{2}{\omega\mu\sigma}\right)^{1/2} = \frac{\lambda_m}{2\pi} \tag{12}$$

into the conductor (Ref 1:53). The symbol δ is known as the skin depth and λ_m is the wavelength of the E-M wave in the conductor.

In reference to Figure 2, if a plane wave is incident on the surface normal, then Snell's Law may be written in the form (Ref 1:58)

$$k_i \sin \theta_i = k_t \sin \theta_t \tag{13}$$

where the subscripts i and t represent the fields in free space and the conductor, respectively.

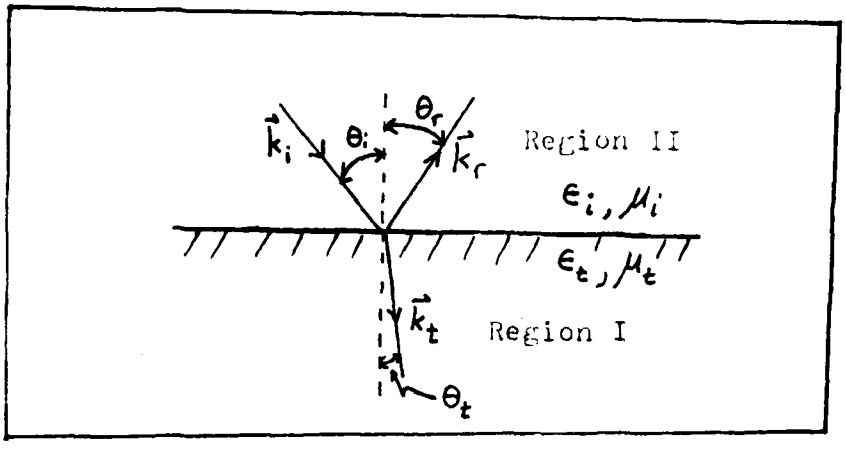

Figure 2. Snell's Law

The wave number, k , is a complex number in general. If k is then defined to be (Ref 1:48)

$$k = k_R - i\, k_I \tag{14}$$

where k_R , called the intrinsic phase constant, is the real part of k , and k_I , called the intrinsic attenuation constant, is the imaginary part of k , then for a

good conductor, $k_R = k_I = (\omega\mu\sigma/2)^{1/2}$ (Ref 1:50). From Eq (5) it is seen that for free space, $k_R = \omega\sqrt{\epsilon_o\mu_o}$ and $k_I = 0$. Eq (13) is now written as

$$\frac{\sin\theta_t}{\sin\theta_i} = \sqrt{\frac{\omega\epsilon_o\mu_o}{\sigma\mu}}\left(\frac{1+i}{\sqrt{2}}\right) \tag{15}$$

Since the permeability μ of a linear medium is approximately equal to μ_o of free space (Ref 1:6) and noting $(i + i)/\sqrt{2} = \sqrt{i}$, then Snell's Law for a free space - good conductor interface is approximated as

$$\frac{\sin\theta_t}{\sin\theta_i} \simeq \sqrt{i\left(\frac{\omega\epsilon_o}{\sigma}\right)} \tag{16}$$

Since for a good conductor $\sigma >> \omega\epsilon$ (for σ of order 10^7, ω of order 10^{14}, and ϵ_o of order 10^{-12}), then Eq (16) implies that the ratio of $\sin\theta_t$ to $\sin\theta_i$ will be very small. For θ_i limited between 0 and $\pi/2$ radians, θ_t must approximately equal zero for arbitrary θ_i . Thus, the rapidly attenuated surface fields propagate very nearly normal (with respect to the surface tangent) into the conductor.

The surface current density in Eq (8) thus produces a tangential electric field given by (Ref 3:18)

$$\hat{n} \times \vec{E}_{tan} = \zeta\, \hat{n} \times \vec{J}_s \tag{17}$$

where $\zeta = \frac{1+i}{\sigma\delta}$ and is called the surface impedance of the conductor. The time-averaged power density dissipated on the surface of the conductor (assuming that the conduction current $\sigma\vec{E}$ is much greater than the displacement current density $\frac{\partial \epsilon \vec{E}}{\partial t}$ —— which is satisfied by the good conductor assumption of $\sigma >> \omega\epsilon$) is then (Ref 1:53)

$$\overline{Q}_{loss} = \text{Re}\left\{\vec{E} \times \vec{H}^*\right\}$$

$$= |H_o|^2 \, \text{Re}\left\{\zeta\right\}$$

$$= \frac{1}{\sigma\delta} |H_o|^2 \quad (\text{watts/m}^2) \qquad (18)$$

where $|H_o|^2 = \vec{H} \cdot \vec{H}^*$ evaluated at the conductor surface and $\text{Re}\{\cdot\}$ means to take the real part only of the expression between the brackets.

It is useful to use the concept of scattering in order to find $\vec{E}$ everywhere so Eq (2') can be used to find $\vec{H}$ for use in Eq (18). The scattered field can be thought of as the field produced by the currents induced on the conductor surface as in Eq (8). This scattered field ($\vec{E}_s$) is thus equal to the difference between the field everywhere with the conductor present ($\vec{E}$) and the incident field with the conductor absent ($\vec{E}^i$) . This is written as (Refl:113)

$$\vec{E}^s = \vec{E} - \vec{E}^i \tag{19}$$

Thus, by solving for $\vec{E}^s$ and given $\vec{E}^i$, $\vec{E}$ is found and Eq (2') then yields $\vec{H}$. The solution for $\vec{H}$ is then used in Eq (18) to give a first approximation of the time-averaged power density dissipated on the highly conductive conductor surface.

The necessary background theory has now been presented to successfully derive the solutions to the specific geometries presented in the next chapter. Since many of the sharp edges occur in highly conductive plane (flat surface) mirrors (see Figure 3), the first geometry discussed in the next chapter is that of an infinite wedge, which has two flat surfaces meeting at a sharp edge. Since present technology is such that perfectly sharp edges are not possible, but in fact the edges are rounded, then the geometry of a parabolic-cylinder is used to approximate flat conductor surfaces with rounded corners. Finally, since waxicons (see Figure 4) are being proposed for use in the resonators of high power chemical lasers, the cone is used to approximate such optical components.

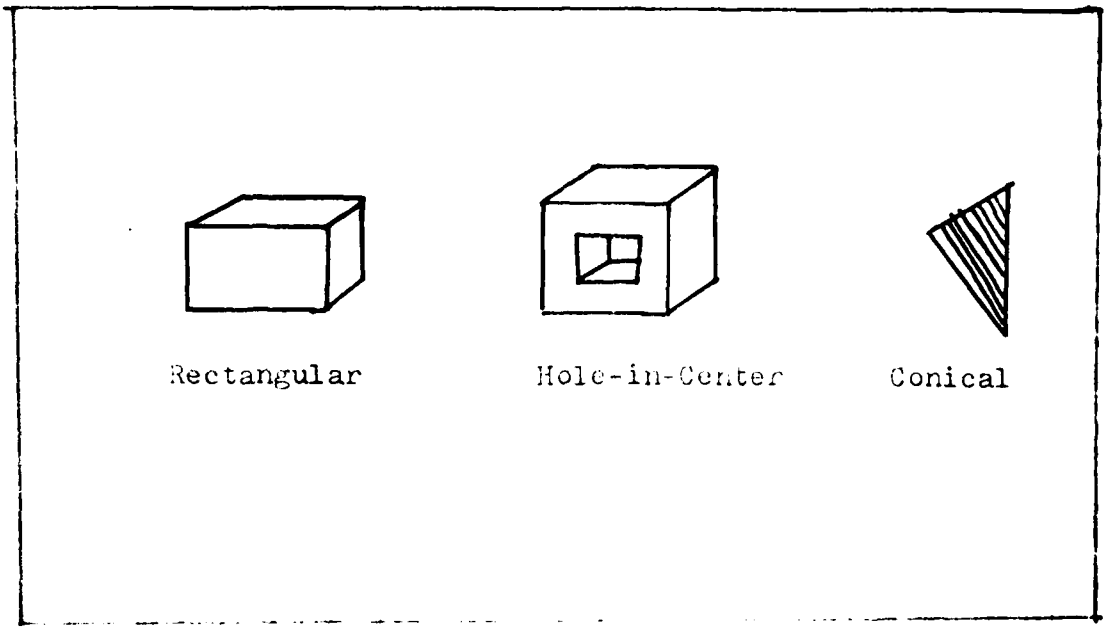

Figure 3. Wedge Configurations

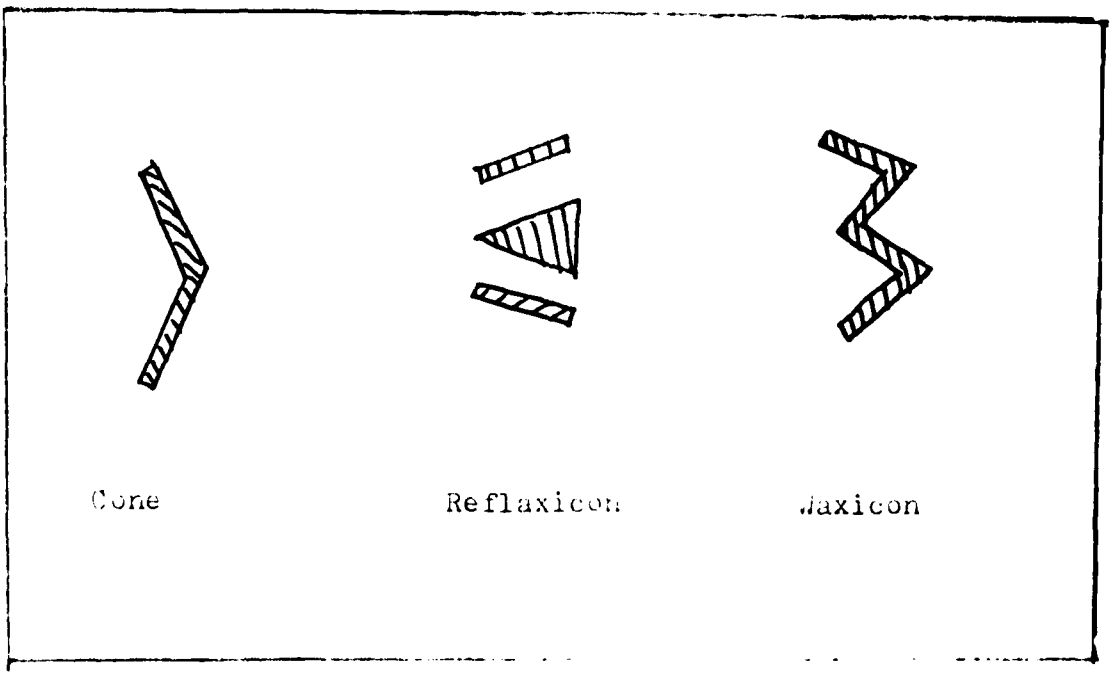

Figure 4. Cone configurations (Ref 10: p 11)

III. Theory Extended to Specific Geometries

The purpose of this chapter is to specialize the theory in the last chapter for specific boundary conditions. The boundary conditions lead to the choice of what coordinate system is used. The first section considers the case of scattering by an infinite, perfectly conducting wedge illuminated by a parallel electric line source. The line source is then moved to infinity so as to approximate plane wave incidence. A first approximation is then made for determining the time-averaged power density dissipated on the surface of a highly conductive wedge. As a special case of the wedge, the half-plane problem using the wedge solution is compared to the classical solution for the half-plane (Born and Wolf's derivation is used; Ref 6:559-570). The method of expanding the infinite wedge problem to one of a finite wedge is introduced.

The second section considers the wave equation for a parabolic-cylindrical coordinate system. Representing a bend with a rounded corner, the parabolic cylinder is discussed; in particular, the difficulty in obtaining numerical results to the solution of the parabolic-cylindrical wave equation is identified. Finally, the last section considers the wave equation for spherical coordinates. A

brief discussion to the solution of the spherical wave equation for a cone boundary (cones have boundaries easily expressed in spherical coordinates) is discussed.

The first section is the most thoroughly discussed section, since the solutions derived are the basis for the next chapter and for the numerical results presented in Chapter V.

Cylindrical Coordinates and the Wedge

The wedge has surfaces that are conveniently expressed in cylindrical coordinates (see Figure 5b). The cylindrical wave equation is introduced first, followed by scattering by wedges. The cylindrical coordinate system used is defined in Figure 5a.

Cylindrical Wave Equation. The scalar version of Eq (7) in cylindrical coordinates with the Laplacian expressed in cylindrical coordinates and $\vec{E}$ replaced by the scalar function ψ is (Ref 1:198)

$$\frac{1}{\rho}\frac{\partial}{\partial\rho}\left(\rho\frac{\partial\psi}{\partial\rho}\right)+\frac{1}{\rho^2}\frac{\partial^2\psi}{\partial\phi^2}+\frac{\partial^2\psi}{\partial z^2}+k^2\psi=0 \qquad (20)$$

Eq (20) is also known as the scalar Helmholtz equation in cylindrical coordinates. If ψ is separable into the form

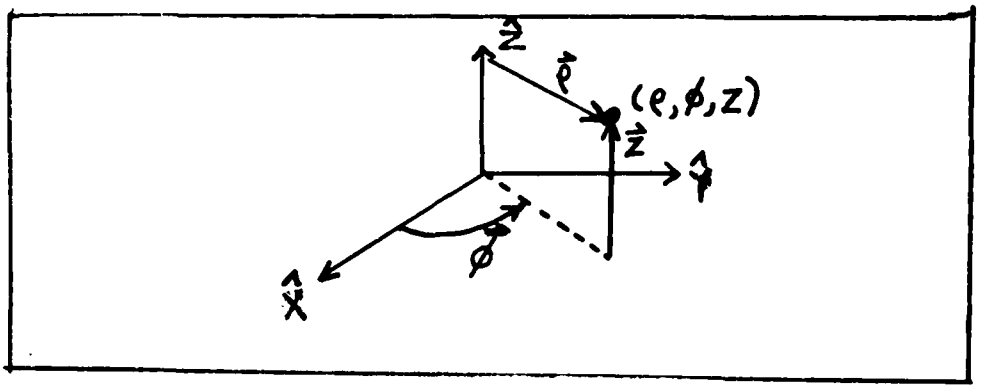

Figure 5a. Cylindrical Coordinate System

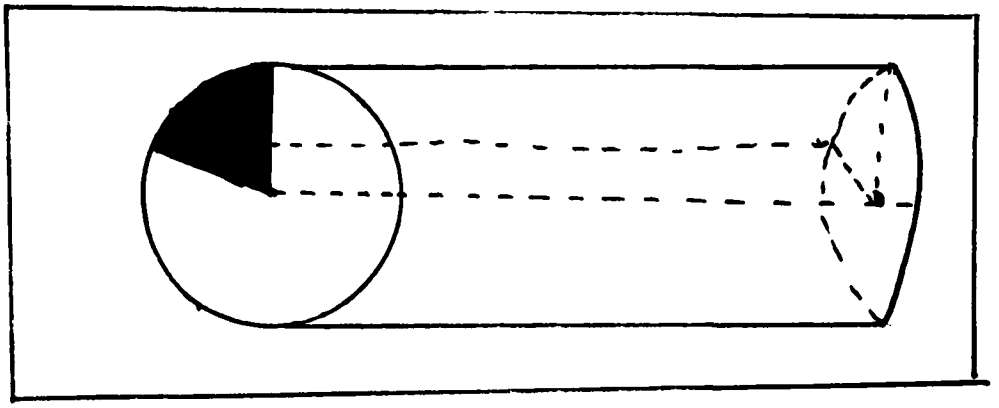

Figure 5b. Wedge as Special Case of Cylinder

$$\Psi(\rho,\phi,z) = \Psi = R(\rho)\Phi(\phi)Z(z) = R\Phi Z \qquad (21)$$

and Eq (20) is assumed to have $e^{i\omega t}$ time dependence, the method of Separation of Variables can be used. The well known separable equations resulting from substitution of Eq (21) into Eq (20) are

$$\frac{d^2Z}{dz^2} + k_z^2 Z = 0 \qquad (22)$$

$$\frac{d^2\Phi}{d\phi^2} + n^2\Phi = 0 \tag{23}$$

$$\rho\frac{d}{d\rho}\left(\rho\frac{dR}{d\rho}\right) + \left[(k_\rho\rho)^2 - n^2\right]R = 0 \tag{24}$$

where k_ρ in Eq (24) is defined by

$$k^2 = k_\rho^2 + k_z^2 \tag{25}$$

Equations (22) and (23) are homogeneous, linear ordinary differential equations with constant coefficients. These give rise to harmonic solutions (sines and cosines). Equation (24) is Bessel's equation of order n and has Bessel function solutions (Ref 1:199). Equation (21) then becomes

$$\psi(\rho,\phi,z) \sim B_n(k_\rho\rho)h(n\phi)h(k_z z) \tag{26}$$

where $h(n\phi)$ and $h(k_z z)$ represent harmonic functions for the solutions of Eqs (23) and (22), respectively. $B_n(k_\rho\rho)$ represents a Bessel function solution to Eq (24) (see Appendix A for the definitions of various Bessel functions). From the principle of superposition, linear combinations of Eq (26) are also solutions to Eq (20). The possible values for n, k_ρ, and k_z are called eigenvalues and any two may be summed or integrated over, except k_ρ and k_z

since they are interrelated by Eq (25). Equation (26) is specified in the discussion to follow.

Scattering by a Wedge. Consider the case of an electric current filament of current I (in amps) located parallel to a perfectly conducting wedge, as shown in Figure 6. The wedge has an angle 2α and covers the space (in cylindrical coordinates ρ, ϕ, z): $2\pi - \alpha \leq \phi \leq \alpha$, $0 \leq \rho < \infty$, and $-\infty < z < \infty$. The filament and wedge are assumed to be imbedded in free space ($\sigma = 0$, $\epsilon = \epsilon_0$, $\mu = \mu_0$). The wedge is assumed to be a linear, isotropic perfect conductor ($\sigma = \infty$). The incident electric field can be described as an outward-traveling cylindrical wave, hence the Hankel function of the second kind and order n (n an integer), denoted by $H_n^{(2)}(k\rho)$, is used (provided $e^{i\omega t}$ time-dependence is assumed) (Ref 1:201). The incident electric

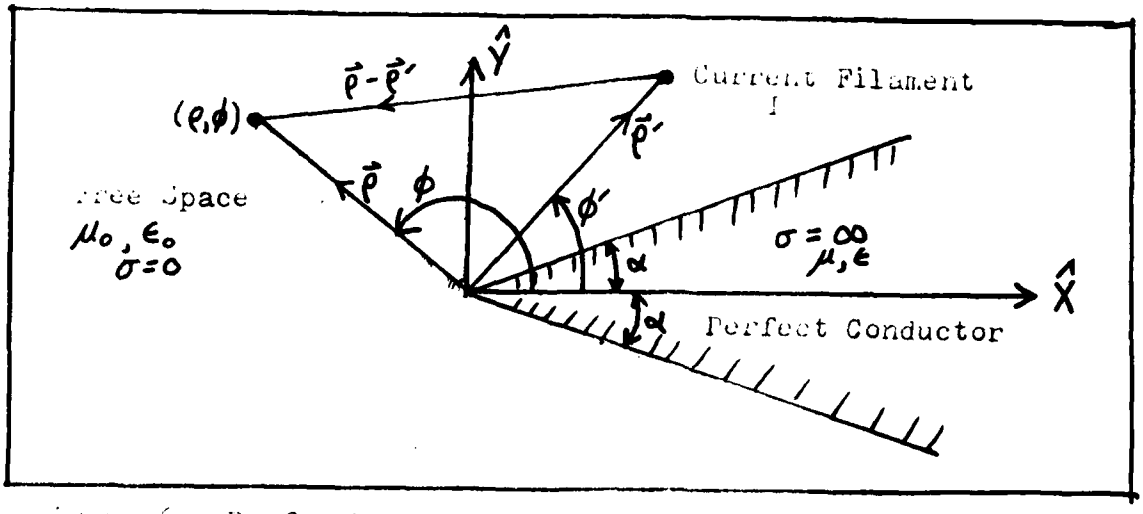

Figure 6. Perfectly conducting wedge near current filament

field is $\hat{z}$-polarized and given by (Ref 1:236)

$$E_z^i = -\frac{k^2 I}{4\omega\epsilon_o} H_o^{(2)}(k|\vec{\rho}-\vec{\rho}'|) \tag{27}$$

where $|\vec{\rho}-\vec{\rho}'| = [\rho^2 + \rho'^2 - 2\rho\rho'\cos(\phi-\phi')]^{1/2}$ and is evident from the geometry in Figure 6.

The addition theorem for Hankel functions is given by (Ref 1:232)

$$H_o^{(2)}(k|\vec{\rho}-\vec{\rho}'|) = \begin{cases} \sum_{n=-\infty}^{\infty} H_n^{(2)}(k\rho') J_n(k\rho) e^{in(\phi-\phi')}, & \rho<\rho' \\ \sum_{n=-\infty}^{\infty} J_n(k\rho') H_n^{(2)}(k\rho) e^{in(\phi-\phi')}, & \rho>\rho' \end{cases} \tag{28}$$

where $J_n(k\rho')$ and $J_n(k\rho)$ are Bessel functions of the first kind of integer order n. Equation (28) substituted into Eq (27) then gives the incident field as

$$E_z^i = \begin{cases} -\frac{k^2 I}{4\omega\epsilon_o} \sum H_n^{(2)}(k\rho') J_n(k\rho) e^{in(\phi-\phi')}, & \rho<\rho' \\ -\frac{k^2 I}{4\omega\epsilon_o} \sum J_n(k\rho') H_n^{(2)}(k\rho) e^{in(\phi-\phi')}, & \rho>\rho' \end{cases} \tag{29}$$

The total electric field everywhere, E_z, is given by Eq (19) as

$$E_z = E_z^i + E_z^s \tag{30}$$

where E_z^i is given by Eq (29) and E_z^s is considered as the field originating from the induced currents on the surface of the wedge and is called the scattered field (Ref 6:558). The scattered electric field is in the form of Eq (29), but with the integer order n changed to real order ν and $J_n(k\rho)$ replaced by $H^{(2)}(k\rho)$. The order ν is determined (to follow later) by the boundary conditions on the wedge surfaces. The scattered electric field E_z^s is then added to the incident electric field E_z^i to yield the total field E_z , as in Eq (30). Since the boundary condition must have $E_z^s = E_z^i$ at the wedge surfaces, the total field must also be $\hat{z}$-polarized (Ref 1:238). The total field is thus written as (Ref 1:238)

$$E_z = \begin{cases} \sum_\nu a_\nu H_\nu^{(2)}(k\rho') J_\nu(k\rho) \sin[\nu(\phi'-\alpha)] \sin[\nu(\phi-\alpha)], & \rho<\rho' \\ \sum_\nu a_\nu J_\nu(k\rho') H_\nu^{(2)}(k\rho) \sin[\nu(\phi'-\alpha)] \sin[\nu(\phi-\alpha)], & \rho>\rho' \end{cases} \tag{31}$$

The boundary conditions that must be imposed on the surfaces of the perfectly conducting wedge are

$$E_z = 0 \quad , \quad \phi = \alpha$$
$$E_z = 0 \quad , \quad \phi = 2\pi - \alpha \tag{32}$$

Solving Eq (31) for the above boundary conditions implies

$$\sin [v(\phi-\alpha)] = 0 \quad , \quad \phi = \alpha \tag{33a}$$

$$\sin [v(\phi-\alpha)] = 0 \quad , \quad \phi = 2\pi - \alpha \tag{33b}$$

Equation (33a) is true for any v, but Eq (33b) is true only for

$$v(2\pi-\alpha-\alpha) = 2v(\pi-\alpha) = m\pi \tag{34}$$

where m is an integer. The value $m = 0$ (thus $v = 0$) is not allowed because E_z in Eq (31) becomes zero for any (ρ, ϕ). The values of m equal to a negative integer are also not allowed, since by the definition of $J_v(k\rho)$ for v negative (see Appendix A), E_z in Eq (31) tends to infinity as k tends to zero. Thus, Eq (34) gives the eigenvalues v of Eq (31) as

$$v = \frac{m\pi}{2(\pi-\alpha)} \quad , \quad m = 1, 2, 3, \ldots \tag{35}$$

The constants a_v are determined by the nature of the source (Ref 1:239). In reference to Figure 7a, the current filament is considered to be an impulse of current of strength I (in amps). Figure 7b represents a vanishingly small

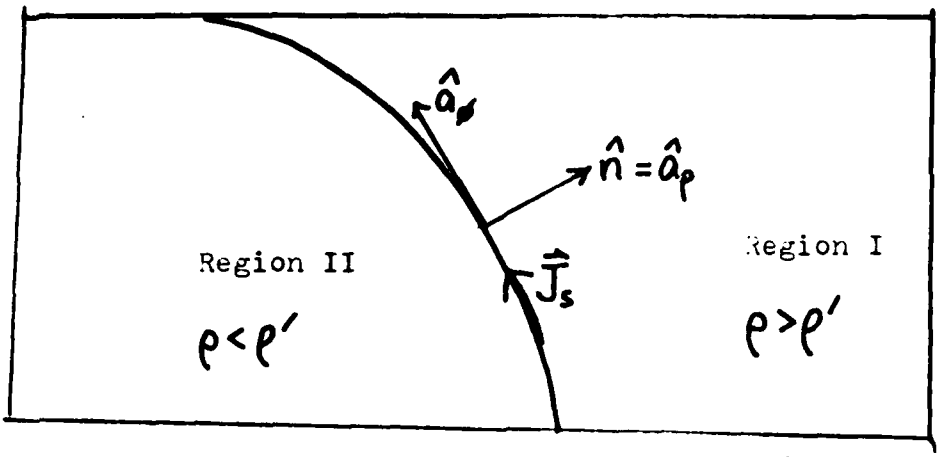

Figure 7a. Surface Current for current filament

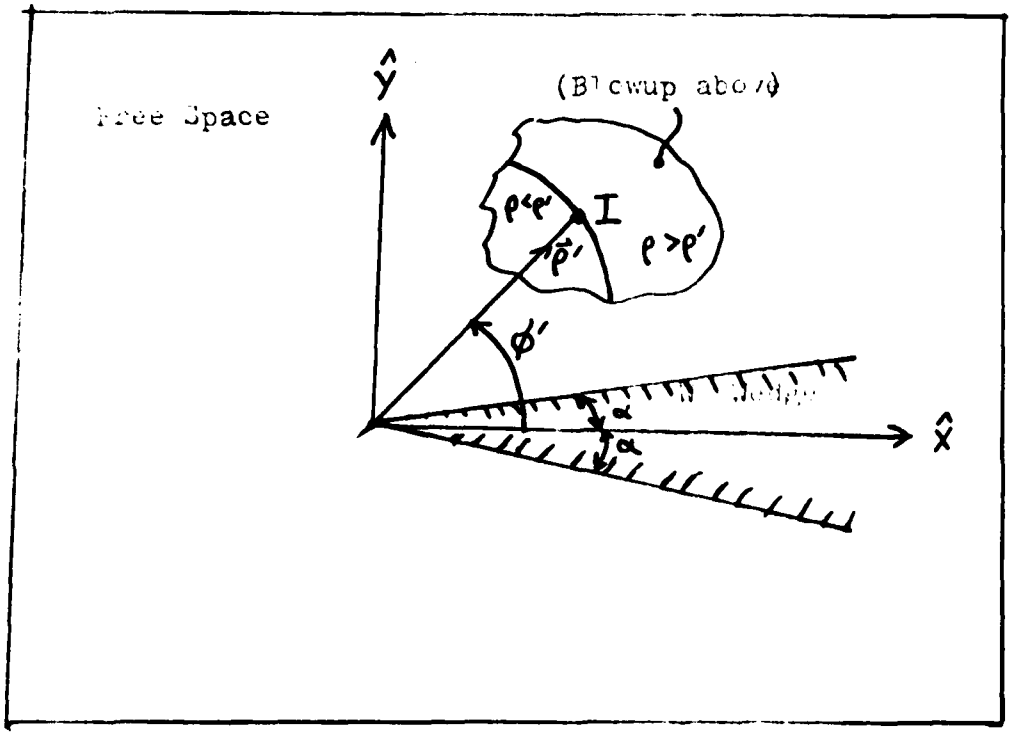

Figure 7b. Impulse Current near wedge

area surrounding the current filament; small enough so that the current filament can be considered as a current sheet ($\rho = \rho'$) separating the regions for $\rho > \rho'$ and $\rho < \rho'$. Appendix B provides the details which, by referring to Figure 7b, leads to the source current density as

$$J_z = -\frac{2}{\pi\omega\mu_o\rho'}\sum_{\nu} a_\nu \sin[\nu(\phi'-\alpha)]\sin[\nu(\phi-\alpha)] \qquad (36)$$

Equation (36) is in the form of a Fourier sine series for the current on $\rho = \rho'$. The Fourier sine series for an impulse of current of strength I (in amps) at $\rho = \rho'$ and $\phi = \phi'$ is given by (Ref 1:239)

$$J_z = \frac{I}{(\pi-\alpha)\rho'}\sum_{\nu} \sin[\nu(\phi'-\alpha)]\sin[\nu(\phi-\alpha)] \qquad (37)$$

Comparing Eq (36) with Eq (37) thus yields

$$a_\nu = -\frac{\omega\mu_o\pi I}{2(\pi-\alpha)} \qquad (38)$$

Of special interest to this thesis is the case of monochromatic plane-wave illumination. This is accomplished by letting the current filament recede to infinity, i.e., $k\rho' \longrightarrow \infty$. The incident electric field in Eq (27) thus becomes (using the large argument approximation for $H_\nu^{(2)}(x)$ as $x \longrightarrow \infty$ given in Appendix A) (Ref 1:240)

$$E_z^i = -\frac{k^2 I}{4\omega\epsilon_o} H_o^{(2)}(k|\hat{\rho}-\hat{\rho}'|)$$

$$\xrightarrow[k\rho'\to\infty]{} -\frac{\omega\mu_o I}{4}\sqrt{\frac{2i}{\pi k\rho'}}\, e^{-ik\rho'} e^{ik\rho\cos(\phi-\phi')} \qquad (39)$$

Equation (39) can thus be written in the form of a plane wave as (Ref 1:240)

$$E_z^i = E_o\, e^{ik\rho\cos(\phi-\phi')}$$

$$\text{where } E_o = -\frac{\omega\mu_o I}{4}\sqrt{\frac{2i}{\pi k\rho'}}\, e^{-ik\rho'} \qquad (40)$$

Only the equation for $\rho < \rho'$ need be considered in Eq (31) to find the electric field E_z everywhere for $k\rho' \longrightarrow \infty$. Using the asymptotic approximation for $H_\nu^{(2)}(k\rho')$ given in Appendix A as (Ref 1:463)

$$H_\nu^{(2)}(k\rho') \xrightarrow[k\rho'\to\infty]{} \sqrt{\frac{2i}{\pi k\rho'}}\; i^\nu e^{-k\rho'} \qquad (A\text{-}12)$$

Eq (31) then becomes

$$E_z \xrightarrow[k\rho'\to\infty]{} \sqrt{\frac{2i}{\pi k\rho'}}\, e^{-ik\rho'} \sum_\nu a_\nu i^\nu J_\nu(k\rho)\sin[\nu(\phi'-\alpha)]\sin[\nu(\phi-\alpha)] \qquad (41)$$

Substitution of a_ν given by Eq (38) and E_o given by Eq (40) into Eq (41) yields

$$E_z = \frac{2\pi E_o}{\pi - \alpha} \sum_{\nu} i^{\nu} J_{\nu}(k\rho) \sin[\nu(\phi' - \alpha)] \sin[\nu(\phi - \alpha)] \quad (42)$$

where ν is given by Eq (35). Equation (42) thus represents the solution of the electric field for a monochromatic, $\hat{z}$-polarized plane wave incident on a perfectly conducting wedge of angle 2α (see Figure 6). The solution for the magnetic field $\vec{H}$ is obtained by applying Maxwell's equation, Eq (2'), to Eq (42), i.e.,

$$\vec{H} = \frac{i}{k}\sqrt{\frac{\epsilon_o}{\mu_o}} \left(\frac{1}{\rho} \frac{\partial E_z}{\partial \phi} \hat{a}_\rho - \frac{\partial E_z}{\partial \rho} \hat{a}_\phi \right) \quad (43)$$

The surface current density, $\vec{J}_s$, is obtained by substituting Eq (43) into

$$\hat{n} \times \vec{H} = \vec{J}_s \quad (10)$$

For the top surface of the wedge, $\hat{n} = \hat{a}_\phi$. The $\hat{a}_\rho$ component of $\vec{H}$ in Eq (43) is the only term used since $\hat{a}_\phi \times \hat{a}_\phi = 0$. The surface magnetic field, denoted by $\vec{H}_s$, is thus given as

$$H_s = \frac{i}{k}\sqrt{\frac{\epsilon_o}{\mu_o}} \frac{1}{\rho} \frac{\partial E_z}{\partial \phi}\bigg|_{\phi = \alpha} \hat{a}_\rho$$

$$= i\sqrt{\frac{\epsilon_o}{\mu_o}} \left(\frac{2\pi E_o}{\pi - \alpha}\right)\left(\frac{1}{k\rho}\right) \sum_{\nu} i^{\nu} \nu J_{\nu}(k\rho) \sin[\nu(\phi' - \alpha)] \hat{a}_\rho \quad (44)$$

where, after differentiating Eq (42) with respect to ϕ, the boundary condition $\phi = \alpha$ was imposed. The surface current density, $\vec{J}_s$, is thus given by

$$\vec{J}_s = J_z \hat{a}_z = - H_{\rho_s} \hat{a}_z$$

$$\text{where } H_{\rho_s} = i\sqrt{\frac{\epsilon_o}{\mu_o}}\left(\frac{2\pi E_o}{\pi-\alpha}\right)\left(\frac{1}{k\rho}\right)\sum_{\nu} i^{\nu}\nu J_{\nu}(k\rho)\sin[\nu(\phi'-\alpha)] \qquad (45)$$

If the wedge is a good conductor of finite conductivity such that $\sigma >> \omega\epsilon$, then Eq (18) of Chapter II is used to obtain a first approximation to the time-averaged power density dissipated on the surface of the wedge, provided that the Leontovich Boundary Condition is satisfied (see Appendix B). It is assumed throughout the rest of this thesis that the Leontovich Boundary Condition is satisfied. Recalling Eqs (12) and (18)

$$\delta = \left(\frac{2}{\omega\mu\sigma}\right)^{1/2} \qquad (12)$$

$$\bar{P}_{loss} = \frac{1}{\sigma\delta}|H_o|^2 \qquad (18)$$

where $|H_o|^2 = H_{\rho_s} \cdot H^*_{\rho_s}$ is the dot product of H_{ρ_s} and its complex conjugate given by Eq (45), thus gives the time-averaged power density loss on the top wedge surface as

$$\overline{P}_{loss} = \frac{\epsilon_o}{\sigma\delta\mu_o}\left(\frac{2\pi E_o}{k\rho(\pi-\alpha)}\right)^2 \cdot \left\{ \sum_v i^v v J_v(k\rho)\sin[v(\phi'-\alpha)] \cdot \sum_v (-i)^v v J_v(k\rho)\sin[v(\phi'-\alpha)] \right\} \quad (46)$$

The problem for the wedge just discussed is for the TM case. The TE case is solved in a similar manner as the TM case, using a magnetic current filament in place of the electric one. For plane wave incidence, the result for the magnetic field is given by (Ref 1:242)

$$H_z = \frac{\pi H_o}{\pi-\alpha} \sum_v \epsilon_v i^v J_v(k\rho)\cos[v(\phi'-\alpha)]\cos[v(\phi-\alpha)]$$

$$\text{where} \quad \epsilon_v = \begin{cases} 1, & v = 0 \\ 2, & v > 0 \end{cases} \quad (47)$$

$$\text{and} \quad v = \frac{m\pi}{2(\pi-\alpha)}, \quad m = 0, 1, 2, \ldots$$

At the top wedge surface ($\phi=\alpha$), the resulting magnetic field on the surface, H_{z_s}, becomes

$$H_{z_s} = \frac{\pi H_o}{\pi-\alpha} \sum_v \epsilon_v i^v J_v(k\rho)\cos[v(\phi'-\alpha)] \quad (48)$$

Substitution of Eq (48) into Eq (10) yields the induced surface current density $\vec{J}_s$ as

$$\vec{J}_s = H_{z_s}\,\hat{a}_\rho = \frac{\pi H_o}{\pi-\alpha}\sum_v \epsilon_v i^v J_v(k\rho)\cos[v(\phi'-\alpha)] \qquad (49)$$

Equations (12) and (18) are used with Eq (48) to obtain a first approximation for the time-averaged power density dissipated on the top surface of the highly conductive wedge. Of note is the differences in the TM case of Eq (44) to the TE case of Eq (48). The TM case of Eq (44) has the term $k\rho$ in the denominator while the TE case of Eq (48) does not. Equation (44) also varies with $\sin[v(\phi'-\alpha)]$ while Eq (48) varies with $\cos[v(\phi'-\alpha)]$. In addition, Eq (48) has an additional $v = 0$ term and slightly different constants.

The TE case is mentioned here only to present the equations necessary to determine the time-averaged power density loss due to TE illumination so as to compare to the TM results presented in Chapter V.

Half-Plane. For $\alpha = 0$, the wedge in Figure 6 reduces to the classical half-plane problem. The half-plane perfect conductor covers the space: $0 \leq x < \infty$, $y = 0$, and $-\infty < z < \infty$; see Figure 8.

It is assumed, in reference to Figure 8, that a monochromatic plane wave (the electric field $\hat{z}$-polarized) is incident at an angle ϕ' on a perfectly conducting half-plane imbedded in free space. The incident electric

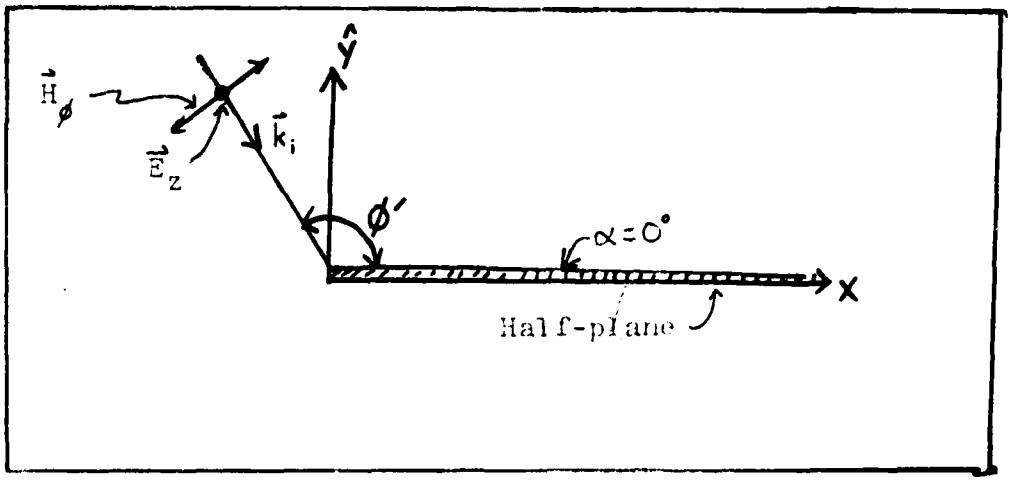

Figure 8. Perfectly conducting half-plane illuminated by z-polarized E and -polarized H.

field is given by Eq (40). The total electric field everywhere is then given by Eq (42) with $\alpha = 0$. The eigenvalues v given in Eq (35) reduce to

$$v = \left.\frac{m\pi}{2(\pi-\alpha)}\right|_{\alpha=0} = \frac{m}{2} \; ; \quad m = (1, 2, 3, \ldots) \qquad (50)$$

The total electric field is then written as

$$E_z = 2 E_o \sum_{m=1}^{\infty} i^{m/2} \cdot J_{m/2}(k\rho) \cdot \sin\left(\frac{m\phi'}{2}\right) \cdot \sin\left(\frac{m\phi}{2}\right) \qquad (51)$$

Specializing Eq (45) for $\alpha = 0$ gives the induced surface current density as

$$\vec{J}_s = J_z \hat{a}_z = -H_{\rho_s} \hat{a}_z \tag{52}$$

where $H_{\rho_s} = i\sqrt{\frac{\epsilon_o}{\mu_o}}\left(\frac{E_o}{k\rho}\right)\sum_{m=1}^{\infty} i^{m/2} \cdot m \cdot J_{\frac{m}{2}}(k\rho)\sin\left(\frac{m\phi'}{2}\right)$

An alternative solution for the half-plane is treated thoroughly by Born and Wolf (Ref 6:559-584). The method involves using dual integral equations for the $\vec{E}$ and $\vec{H}$ fields, of which dual is meant that a single unknown function satisfies different equations for two distinct ranges of parameter (Ref 6:564-565). The final result is Sommerfeld's equation (Ref 6:569)

$$E_z = \frac{e^{i\pi/4}}{\sqrt{\pi}} E_o \left\{ e^{ik\rho\cos(\phi-\phi')} \cdot F(a_1) - e^{ik\rho\cos(\phi-\phi')} \cdot F(a_2) \right\}$$

where $F(a) = \sqrt{\frac{\pi}{2}}\left\{\left[\frac{1}{2} - C\left(\sqrt{\frac{2}{\pi}}a\right)\right] - i\left[\frac{1}{2} - S\left(\sqrt{\frac{2}{\pi}}a\right)\right]\right\}$

and $a_1 = -\sqrt{2k\rho}\cos\left(\frac{\phi-\phi'}{2}\right)$

$a_2 = -\sqrt{2k\rho}\cos\left(\frac{\phi+\phi'}{2}\right)$ (53)

where $C\left(\sqrt{\frac{2}{\pi}}a\right)$ and $S\left(\sqrt{\frac{2}{\pi}}a\right)$ are the Fresnel cosine and sine integrals, respectively, and defined as (Ref 5:300)

$$C(x) = \int_0^x \cos\left(\frac{\pi}{2} t^2\right) dt$$

$$S(x) = \int_0^x \sin\left(\frac{\pi}{2} t^2\right) dt \qquad (54)$$

Equation (53) is valid for the incident field E_z^i given by Eq (40). (Born and Wolf used $E_z^i = \exp[-ik\rho \cos(\phi - \phi')]$) and for E_o normalized to equal one.

By using Maxwell's equation, Eq (2') again, and the boundary condition Eq (8) to get the surface current density, then

$$J_{s_{BW}} = J_z \hat{a}_z = -H_{\rho_s} \hat{a}_z$$

where $$H_{\rho_s} = \sqrt{\frac{\epsilon_o}{\mu_o}} \left(\frac{e^{i\pi/4} E_o}{\sqrt{\pi}}\right) e^{-ik\rho} \left\{ i\sqrt{\frac{2}{k\rho}} \sin\left(\frac{\phi'}{2}\right) - 2 \sin\phi' \sqrt{\frac{\pi}{2}} e^{iu^2} \left[\frac{1}{2} - C(a) + i\left(S(a) - \frac{1}{2}\right)\right] \right\}$$

and $$u = -\sqrt{2k\rho} \cos(\phi'/2)$$

$$a = \sqrt{\frac{2}{\pi}}\, u \qquad (55)$$

In the next chapter, a truncated version of Eq (52) is compared numerically on the computer against Eq (55) so as to give a clue on the reliability of the truncation and Bessel function subroutine. To get an indication of the reliability of the numerical results presented in Chapter V and based on Eq (46) for the wedge, a comparison of

$\vec{J}_s \cdot \vec{J}_s^*$ of Eq (52) is compared against $\vec{J}_s \cdot \vec{J}_s^*$ of Eq (55). For future reference in Chapter IV, these equations are denoted by

$$\left|\vec{J}_s\right|^2_H = \vec{J}_s \cdot \vec{J}_s^* \qquad (52')$$

for $\vec{J}_s$ given by Eq (52) and

$$\left|\vec{J}_s\right|^2_{BW} = \vec{J}_s \cdot \vec{J}_s^* \qquad (55')$$

for $\vec{J}_s$ given in Eq (55).

As an additional check on the reliability of a computer routine for the truncation of Eq (45) (since computers can't compute infinite sums), the case of $\alpha = 90°$ is examined. This is simply the case of a plane wave in free space incident on the surface (the entire $\hat{y}$ - $\hat{z}$ plane with x = 0) of a perfect conductor (see Figure 9).

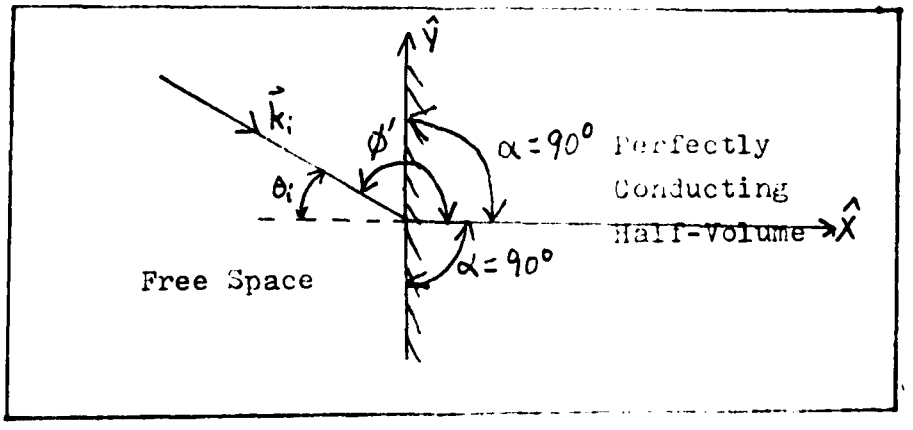

Figure 9. Perfectly conducting half-volume

For $\alpha = 90°$, Eq (35) for v reduces to

$$v = \left.\frac{m\pi}{2(\pi-\alpha)}\right|_{\alpha=\frac{\pi}{2}} = m \quad , \quad m = (1,2,3,\ldots) \qquad (56)$$

and Eq (45) for $\alpha = \pi/2$ reduces to

$$H_{\rho_s} = i\sqrt{\frac{\epsilon_o}{\mu_o}}\left(\frac{4E_o}{k\rho}\right)\sum_{m=1}^{\infty} i^m \cdot m \cdot J_m(k\rho)\sin\left[m\phi' - \frac{m\pi}{2}\right] \qquad (57)$$

Using cartesian coordinates, the classical solution to this problem is (Ref 16:473, 531)

$$\overline{\rho}_{loss} = \sqrt{\frac{\epsilon_o}{\mu_o}} E_o^2 \cos^2\theta_i \qquad (58)$$

where θ_i is the angle of incidence with respect to the surface normal ($\theta_i = \phi' - \pi$) . Comparison of Eq (58) with Eq (57) implies $H_{\rho_s} = H_{y_s}$ (evident from Figure 9 is that $\hat{a}_\rho$ is in the $\hat{a}_y$ direction on the conductor surface). A truncated version of Eq (57) is compared numerically to Eq (58) in the next chapter.

Extension to Three Dimensions. Now consider the wedge in Figure 10 that covers the space: $0 \leq \rho < \infty$, $2\pi - \alpha \leq \phi \leq \alpha$, $z_1 \leq z \leq z_2$. It has the same geometry as the wedge in Figure 6, except that now the wedge is finite along the $\hat{z}$-axis . Thus, a three-dimensional wave

equation must be solved instead of the simpler two-dimensional wave equation for the case of non-varying geometry with respect to the z-axis. However, by applying a Fourier transformation with respect to the z-axis, the three-dimensional wave equation can be reduced to a two-dimensional wave equation.

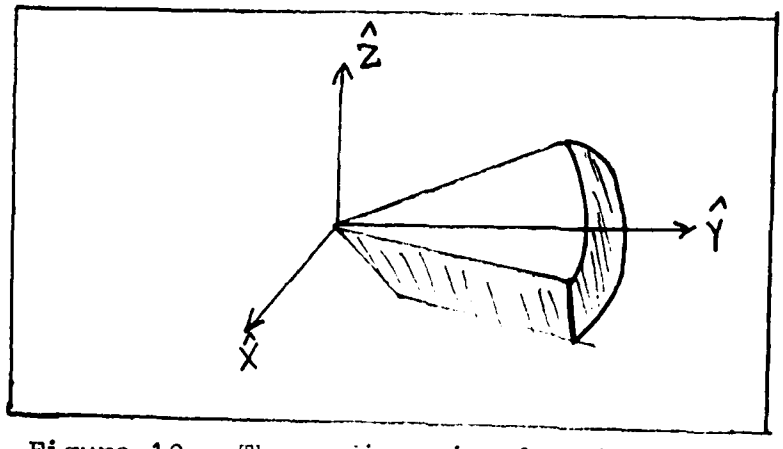

Figure 10. Three-dimensional wedge

As an example of this, if $\psi(\rho,\phi,z)$ is a solution to the three-dimensional wave equation

$$\nabla^2\psi + k^2\psi = 0 \quad ,$$

then $\Psi(\rho,\phi,w) = \int_{-\infty}^{\infty}\psi(\rho,\phi,z)\, e^{-iwz}dz$ is a solution to the two-dimensional wave equation

$$\nabla^2 \Psi + K^2 \Psi = 0$$

where $K^2 = k^2 - w^2$ (Ref 1:243). When the two-dimensional wave equation above is solved for Ψ, then ψ may be solved using the inversion (Ref 1:243)

$$\psi(\rho, \phi, z) = \frac{1}{2\pi} \int_{-\infty}^{\infty} \Psi(\rho, \phi, w) e^{iwz} dw \qquad (59)$$

Parabolic Cylinder

Since technology has not advanced yet to the stage of producing perfectly sharp edges, the parabolic cylinder is useful to approximate a rounded corner. The two-dimensional parabolic-cylindrical coordinate system is shown in Figure 11. The $\hat{z}$-axis is perpendicular to the plane of the paper. The transformation from rectangular coordinates (x,y,z) to parabolic-cylindrical coordinates (u,v,z) is given in Figure 11.

The wave equation that must be solved, Eq (7), in parabolic-cylindrical coordinates is (Ref 7:282)

$$\frac{1}{c^2(u^2+v^2)} \left(\frac{\partial^2 \psi}{\partial u^2} + \frac{\partial^2 \psi}{\partial v^2} \right) + \frac{\partial^2 \psi}{\partial z^2} + k^2 \psi = 0 \qquad (60)$$

where $\psi(u,v,z) = \psi$ replaces the vector $\vec{E}$. Assuming $\psi(u,v,z)$ is separable, i.e.,

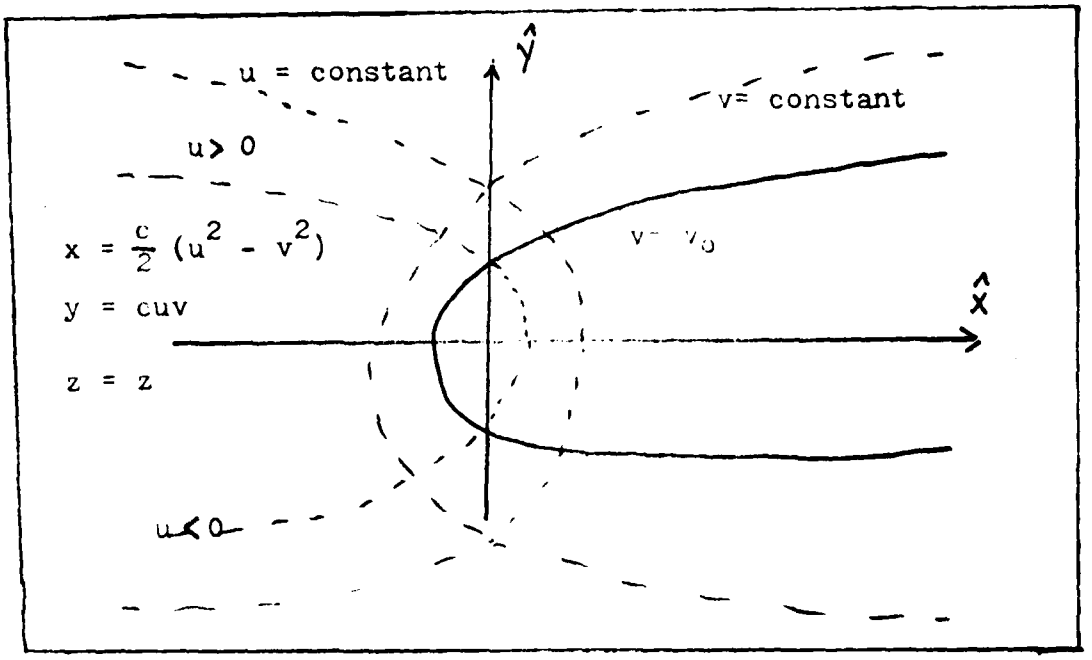

Figure 11. Parabolic cylinder at $v = v_0$

$$\Psi(u,v,z) = U(u)V(v)Z(z) \tag{61}$$

then the method of Separation of Variables yields the three differential equations (see Appendix B for details)

$$\frac{d^2Z}{dz^2} + k_z^2 Z = 0 \tag{62}$$

$$\frac{d^2U}{du^2} + (2\nu + 1 - u^2)U = 0 \tag{63}$$

$$\frac{d^2V}{dv^2} + \left[-(2\nu+1) - v^2\right]V = 0 \tag{64}$$

Equation (62) is the harmonic equation discussed earlier, leading to linear combinations of cosines and sines. These solutions are bounded for $-\infty < z < \infty$. Equation (62) has as a general solution (Ref 7:294)

$$U(u) = Ae^{-k_z c u^2/2} H_\nu(\sqrt{k_z c}\, u) + Be^{k_z c u^2/2} H_{-\nu-1}(i\sqrt{k_z c}\, u) \tag{65}$$

where k_z is given in Appendix B and $H_\nu(\cdot)$ is called the Hermite function of degree ν and defined in Appendix A.

The solution to Eq (65) must be bounded for u approaching $\pm\infty$. Using the asymptotic expansions for $H_\nu(ix)$ and $H_{-\nu-1}(ix)$ given in Appendix A thus forces B in Eq (65) to equal zero and ν to equal non-negative integers. Thus, the condition of finite U(u) forces Eq (65) to become

$$U(u) = A\, e^{-k_z c u^2/2} \cdot H_n(\sqrt{k_z c}\, u) \quad , \; n = (0,1,2,3,\ldots) \tag{65'}$$

With the restriction of $\nu = n = (0,1,2,3,\ldots)$, Eq (64) has the general solution (Ref 7:294)

$$V(v) = Pe^{k_z c v^2/2} H_n(i\sqrt{k_z c}\, v) + Q e^{-k_z c v^2/2} H_{-n-1}(\sqrt{k_z c}\, v) \qquad (66)$$

Using the asymptotic expansions for $H_n(ix)$ and $H_{n-1}(x)$ given in Appendix A and the fact that $V(v)$ must be bounded, yields

$$V(v) = Q\, e^{-k_z c v^2/2} \cdot H_{-n-1}(\sqrt{k_z c}\, v) \quad , \; n = (0,1,2,3\ldots) \qquad (66')$$

The surface of the conductor (see Figure 11) is at $v = v_0$. The boundary condition that must be satisfied is then

$$\psi = 0 \quad , \quad v \leq v_0 \qquad (67)$$

Using superposition of the solutions to Eqs (62), (63), and (64), setting $z = 0$ for the two-dimensional problem, and combining the constant A in Eq (65') with the constant Q in Eq (66') to make $Q_{m,n}$, then Eq (67) forces

$$0 = \sum_{m=0}^{\infty} \sum_{n=0}^{\infty} Q_{m,n} H_n(\sqrt{k_z c}\, u) H_{-m-1}(\sqrt{k_z c}\, v_o) \qquad (68)$$

It is necessary to find the coefficients $Q_{m,n}$ for each m and n that satisfy Eq (68) in order to complete the solution to Eq (60). The boundary condition of Eq (67) forces the conditions of Eq (68). Finding solutions to $Q_{m,n}$ on a computer presents a more difficult problem than that of Eq (45).

Spherical Coordinates and the Cone

In this section, the spherical wave equation is solved and the solution for the boundary conditions of a perfectly conducting cone are briefly discussed. The spherical coordinate system to be used, with coordinates (r,θ,ϕ), is defined in Figure 12.

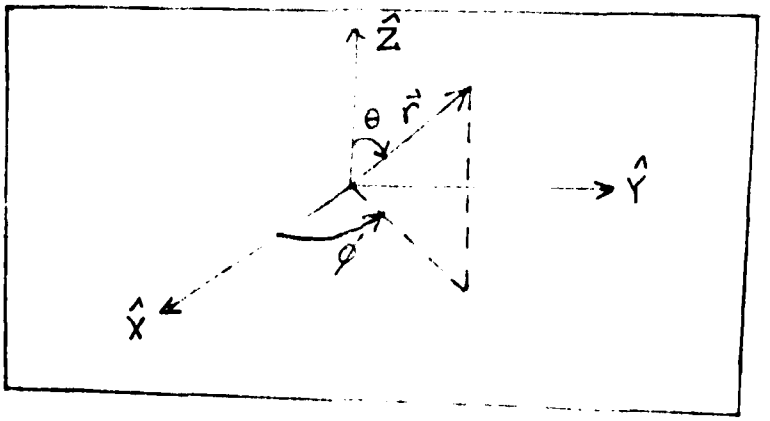

Figure 12. Spherical Coordinate System

Spherical Wave Equation. The scalar Helmholtz equation in spherical coordinates is given by (Ref 1:264)

$$0 = \frac{1}{r^2}\frac{\partial}{\partial r}\left(r^2\frac{\partial \psi}{\partial r}\right) + \frac{1}{r^2\sin\theta}\frac{\partial}{\partial \theta}\left(\sin\theta\frac{\partial \psi}{\partial \theta}\right) + \frac{1}{r^2\sin^2\theta}\frac{\partial^2\psi}{\partial \phi^2} + k^2\psi \tag{69}$$

Assuming $\psi(r,\theta,\phi)$ is separable, i.e.

$$\psi(r,\theta,\phi) = \psi = R(r)\Theta(\theta)\Phi(\phi) = R\Theta\Phi \tag{69'}$$

then the method of Separation of Variables yields the three differential equations (Ref 1:265)

$$\frac{d^2\Phi}{d\phi^2} + m^2\Phi = 0 \tag{70}$$

$$\frac{d}{dr}\left(r^2\frac{dR}{dr}\right) + \left[k^2r^2 - n(n+1)\right]R = 0 \tag{71}$$

$$\frac{1}{\sin\theta}\frac{d}{d\theta}\left(\sin\theta\frac{d\Theta}{d\theta}\right) + \left[n(n+1) - \frac{m^2}{\sin^2\theta}\right]\Theta = 0 \tag{72}$$

Equation (70) is the harmonic equation seen in the previous two sections. Its solutions are denoted by $h(m\phi)$. Equation (71) is closely related to Bessel's equation as in Eq (24) of the first section. It has solutions that are called spherical Bessel functions. Denoting the ordinary Bessel functions by $B_n(kr)$ and $b_n(kr)$ for

the spherical Bessel functions, the relation between the two is given by (Ref 1:265)

$$b_n(kr) = \sqrt{\frac{\pi}{2kr}}\, B_{n+\frac{1}{2}}(kr)$$

Equation (72) is related to Legendre's equation and gives rise to associated Legendre solutions (see Appendix A), denoted by $L_h^m(\cos\theta)$ (Ref 1:265).

The solution to ψ in Eq (69) is therefore written as a linear combination of

$$\psi(r,\theta,\phi) = h(m\phi)b_n(kr)L_n^m(\cos\theta) \qquad (73)$$

Cone. Figure 13a represents a finite perfectly conducting cone imbedded in free space and Figure 13b represents an infinite perfectly conducting cone imbedded in free space. Both cones have conductor surfaces easily expressed in spherical coordinates.

Rogers, Schindler, and Schultz (Ref 8:67-80) have obtained numerical results from a computer for the case of a monochromatic plane wave (electric field $\hat{x}$-polarized) incident head on the tip of the cone in Figure 13a (propagating in the $-\hat{z}$ direction). The boundary conditions that must be satisfied include (Ref 8:70)

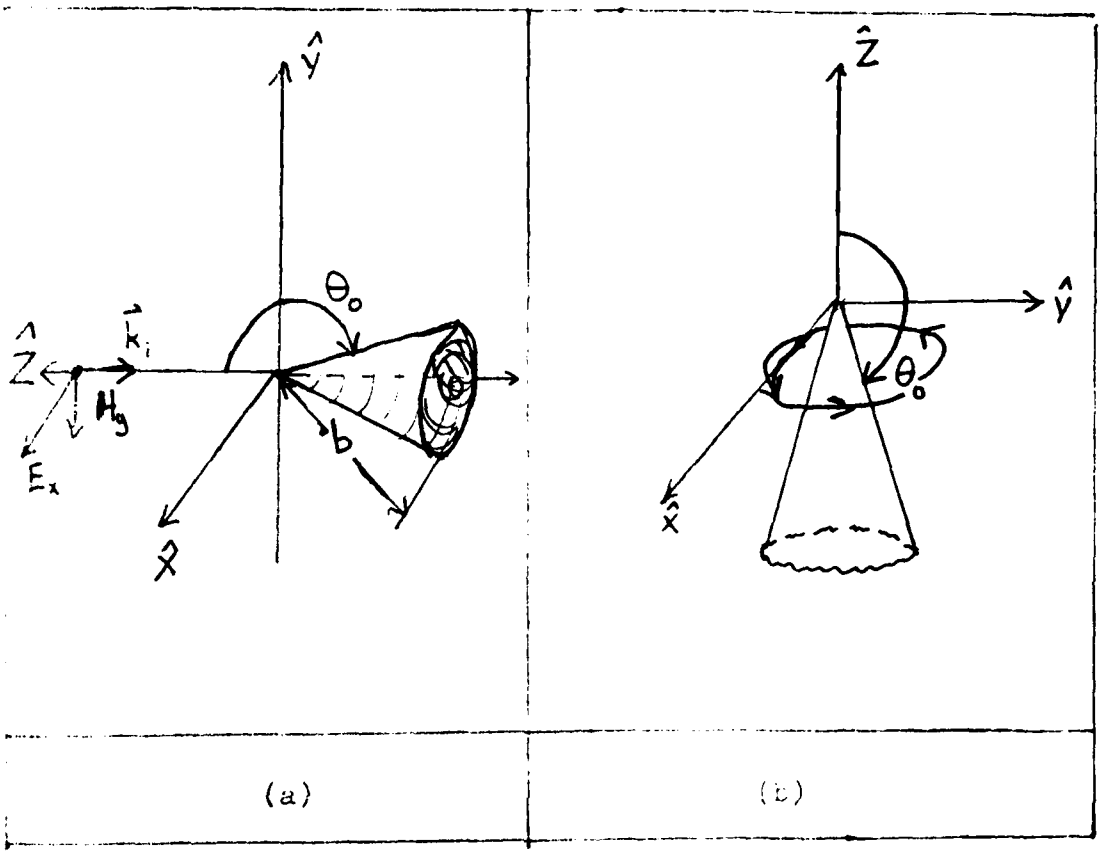

Figure 1. (a) Finite cone illuminated by plane wave
(b) Infinite cone illuminated by ring source

$$\vec{E} = 0 \quad , \quad \theta = \theta_o \quad \text{and} \quad r \leq b$$

and finite energy at the edge of the cone ($r \longrightarrow b$, $\theta \rightarrow \theta_o$).

Harrington (Ref 1:303-306) examines the case of a uniform $\hat{\phi}$-directed ring source illuminating an infinite cone as in Figure 13b. The boundary conditions that must be satisfied include (Ref 1:303)

$$\vec{E} = 0 \quad , \quad \theta = \theta_o$$

and that the energy remain bounded (finite). The boundary conditions for the cone in both cases require that (Ref 1: 304 and Ref 8:72)

$$\left[\frac{d}{d\theta} P_v(\cos\theta)\right]_{\theta=\theta_o} = 0 \tag{74}$$

where $P_v(\cos\theta)$ is called the associated Legendre function of the first kind of order v (see Appendix A for a definition). The important point here is that the physical boundaries of the cone geometry force the condition in Eq (74) to be true. Numerical calculations are difficult to obtain for $\vec{E}$ because of the problem of obtaining the eigenvalues v and the eigenfunctions $P_v(\cos\theta)$ in Eq (74) (Ref 1:305 and Ref 8:77).

IV. Verification of Routines

Introduction

The purpose of this chapter is to verify a Bessel function computer subroutine able to fulfill the requirements of the criteria established in the following sections. Equation (46) is the key equation in support of the main objective of this thesis. It involves fractional order Bessel functions of the first kind. Though many reliable computer subroutines are available for integer order Bessel functions and spherical (order of odd multiples of one-half) Bessel functions of the first kind, not many are available to calculate fractional order Bessel functions. Equation (46) involves an infinite summation. Since computers can only compute finite sums, it is necessary to truncate Eq (46) in such a way that the terms truncated off are insignificant compared to the finite sum. For higher arguments of the Bessel function (on the order of one hundred), orders greater than the argument are needed before the value of the Bessel functions fall off appreciably. Therefore, it is also necessary to find a computer subroutine that calculates high order (and fractional) Bessel functions of the first kind. The availability of reliable computer subroutines of this kind is still further reduced. The

necessity of finding such a subroutine is thus of the utmost importance.

A thorough literature check has revealed no numerical results for the time-averaged power density loss dissipated on the surface of a conducting wedge near the vicinity of its edge. Thus, there isn't any data to check the results of a truncation of Eq (46) against. The next chapter presents numerical results for a truncated version of Eq (46). In order to accept these results as valid, alternative checks must be made. One method involves verifying the Bessel function subroutine for the range of argument and order established in the criteria of the next section. Another method involves the half-plane problem discussed in the previous chapter. Equation (46), for the wedge, and Eq (52'), for the half-plane, are very similar in nature. Both equations involve an infinite sum containing a Bessel function of the first kind of increasing order (fractional and/or integer). They are also both multiplied by $[(\sqrt{-1})^{\text{order}} \cdot (\text{order}) \cdot \sin(\text{order} \cdot \text{constant})]$, where the word "order" represents the value of the order. The order is the increasing index of the summation. A finite summation version of Eq (52') for the half-plane is compared against the classical solution (from Born and Wolf) of Eq (55'). Thus, because of the similarity in nature of Eqs (46) and (52'), it is

hoped that the results of Eq (46) presented in the next chapter can be accepted as valid.

Criteria and Results for Verifying Bessel Function Subroutine

This section provides support to verify a Bessel function subroutine that produces Bessel functions of the first kind, given by $J_{\nu+N}(k\rho)$, for use in Eqs (45) and (46), where ν is the fractional part of the order and N is the integer part of the order.

The argument of the Bessel function is $k\rho$, where k is the wavenumber given by Eq (5) in Chapter II, and ρ is the radial distance from the edge to the point of interest. Since the main objective of this thesis is to find the time-averaged power density dissipated on the surface of a highly conducting infinite wedge (of angle 90°) near the vicinity of the edge, it is necessary to establish the range of $k\rho$. Atomic distances (radius of atoms, bond lengths between atoms making up a molecule, etc.) range around the order of one angstrom ($1\text{Å} = 10^{-10}$ meters). The radius of a copper ion (+1) is 0.96Å, for example (Ref 4:F-171). Since the incident radiation of interest is a monochromatic plane-wave in the micron wavelength range, a value of $k\rho = 0.001$ represents a point $\rho \simeq 0.000159$ wavelengths (of the incident radiation) from the edge. For a CO_2 laser of $\lambda = 10.6$ microns ,

ρ is then equal to approximately 16.9Å away from the edge, which is closer to the edge than what present technology can probably make for a sharp corner of a plane, flat mirror. Increasing $k\rho$ by a factor of 10^5 ($k\rho = 100$) gives the point $\rho \simeq 15.9$ wavelengths away from the edge, or $\rho \simeq 169$ microns = 0.169 mm for $\lambda = 10.6$ microns. Thus, by choosing the range $0.001 \leq k\rho \leq 100$, an adequate range is provided for investigating the power density dissipated on the surface of a highly conductive infinite wedge near the vicinity of the edge. The Bessel function subroutine must be verified, therefore, for a range of argument $0.001 \leq k\rho \leq 100$ (Note: Another very important reason for choosing the upper bound of $k\rho = 100$ is that the Bessel function subroutine requires a large amount of computer memory and time when computing large orders for arguments greater than 100 or so. Appendix C describes the basic theory behind the Bessel function subroutine used).

Equations (45) and (46) for the wedge involve an infinite summation. Since the computer can only evaluate finite summations, an approximation of Eqs (45) and (46) must be made by truncating the infinite summation. The truncated-off terms must be small enough so as to be insignificant if all of them were added to the finite summation approximation. Recalling that the Bessel function of concern involves an order having an integer

part, N , and a fractional part, ν , it is necessary to truncate the summation at some maximum integer order, N_{max} . The condition chosen on N_{max} is such that for any integer M greater than N_{max} , the absolute value of $J_{\nu+M}(k\rho)$ must be less than 10^{-10}, i.e.

For $J_{\nu+N}(k\rho)$,

$$\text{where } 0.001 \leq k\rho \leq 100 \quad ; \quad k\rho \text{ real}$$
$$0 \leq \nu < 1 \quad ; \quad \nu \text{ real}$$
$$N = (0,1,2,3,\ldots,N_{max}) \tag{75}$$

then for any integer $M > N_{max}$

$$\left|J_{\nu+M}(k\rho)\right| < 10^{-10}$$

The condition for $\left|J_{\nu+M}(k\rho)\right| < 10^{-10}$ is chosen for reasons discussed in Appendix B. The above conditions, Eq (75), are true for all the criteria presented in this chapter.

The criteria can now be established to determine the validity of the Bessel function subroutine for the range of argument and order given in Eq (75).

Criterion (IV-1). For the range of argument and order given in Eq (75), then require

$$\left| \frac{J_{\nu+N}(k\rho)\big|_{SUB} - J_{\nu+N}(k\rho)\big|_{STD}}{J_{\nu+N}(k\rho)\big|_{STD}} \right| < 10^{-5}$$

where the value of $J_{\nu+N}(k\rho)$ calculated by the subroutine is denoted by $J_{\nu+N}(k\rho)\big|_{SUB}$ and the value of $J_{\nu+N}(k\rho)$ given by accepted, published values is denoted by $J_{\nu+N}(k\rho)\big|_{STD}$.

The value of 10^{-5} relative error was chosen rather arbitrarily since it is difficult to predict what the computer round-off error and addition of absolute error, due to the summation in Eqs (45) and (46), will come out as. Round-off error is defined as the error taking into account the truncation of an infinite summation and the inherent error due to rounding off the values of terms other than the Bessel function in Eqs (45) and (46). The round-off error, if a problem, will become evident in the half-plane check in the next section.

As a check to see how the absolute error of the Bessel function subroutine adds up in a summation, use is made of the following relations (Ref 5:301, 361)

$$C\left(\sqrt{\tfrac{2}{\pi}x}\right) = \int_0^{\sqrt{\frac{2}{\pi}x}} \cos\left(\tfrac{\pi}{2}t^2\right) dt = \sum_{N=0}^{\infty} J_{2N+\frac{1}{2}}(x) \qquad (76a)$$

$$S\left(\sqrt{\frac{2}{\pi}x}\right) = \int_0^{\sqrt{\frac{2}{\pi}x}} \sin\left(\frac{\pi}{2}t^2\right)dt = \sum_{N=0}^{\infty} J_{2N+\frac{3}{2}}(x) \qquad (76b)$$

$$1 = J_0(x) + 2\sum_{N=1}^{\infty} J_{2N}(x) \qquad (77)$$

where $C\left(\sqrt{\frac{2}{\pi}x}\right)$ and $S\left(\sqrt{\frac{2}{\pi}x}\right)$ are commonly known as the Fresnel cosine and sine integrals, respectively. For computational reasons discussed earlier, the infinite sums in Eqs (76a), (76b), and (77) must be truncated to N_{max}, where N is defined as in Eq (75). Even though Eqs (76a), (76b), and (77) involve only the summation of Bessel functions of integer order or of integer plus one-half order while Eqs (45) and (46) involve the summation of Bessel functions of any fractional order, Eqs (76a), (76b), and (77) provide both a worst case and best case for $x \geq 10$. For $x < 10$, the accuracy will depend on computer memory requested (see Appendix C). The Bessel function routine, for $x \geq 10$, provides better accuracy for fractional orders approaching one-half than for fractional orders approaching zero or one (see Appendix C). As a result, Eqs (76a) and (76b) provide the best case for checking for accuracy and Eq (77) provides the worst case.

Criterion (IV-2a). For the range of argument and order given in Eq (75), then require

$$\left| \frac{C\left(\sqrt{\frac{2}{\pi}}k\rho\right) - \sum_{N=0}^{N_{max}} J_{2N+\frac{1}{2}}(k\rho)}{C\left(\sqrt{\frac{2}{\pi}}k\rho\right)} \right| < 10^{-3}$$

where $C\left(\sqrt{\frac{2}{\pi}}k\rho\right)$ denotes accepted, published values of the Fresnel cosine integral and the summation is the truncated version of Eq (76a). N_{max} in this case is equal to the even value of $2N$ where the summation is truncated.

Criterion (IV-2b). For the range of argument and order given in Eq (75), then require

$$\left| \frac{S\left(\sqrt{\frac{2}{\pi}}k\rho\right) - \sum_{N=0}^{N_{max}} J_{2N+\frac{3}{2}}(k\rho)}{S\left(\sqrt{\frac{2}{\pi}}k\rho\right)} \right| < 10^{-3}$$

where $S\left(\sqrt{\frac{2}{\pi}}k\rho\right)$ denotes accepted, published values of the Fresnel sine integral and the summation is the truncated version of Eq (76b). N_{max} in this case is equal to the odd value of $2N+1$ where the summation is truncated.

Criterion (IV-3). For the range of argument and order given in Eq (75), then require

$$\left| 1 - \left[J_0(k\rho) + 2 \sum_{N=1}^{N_{max}} J_{2N}(k\rho) \right] \right| < 10^{-3}$$

where the expression in the square brackets is the truncated version of Eq (77). N_{max} in this case is equal to the even value of $2N$ where the summation is truncated.

As in Criterion (IV-1), the relative error for the most recently presented criteria was chosen rather arbitrarily since it is hard to predict if the round-off error will be a problem. The next section (involving the half-plane) offers a better indicator on how (in)significant the round-off error is.

Results. The following tables are results of computer runs to test the criteria presented so far in this chapter. Only a few of the hundreds of values tested are presented in these tables (additional tables are in Appendix D). The range of order and argument, however, is limited by the non-availability of published tables to compare against (see Appendix D).

Table (IV-1) is in reference to Criterion (IV-1) (two additional tables are in Appendix D). The column

labeled Relative Error gives the absolute value of the error given in Criterion (IV-1). As evidenced by Table (IV-1), the maximum relative error between the subroutine value and the accepted value is less than 10^{-6}. The additional tables presented in Appendix D also have maximum relative errors less than 10^{-6}. All the values produced by the subroutine that were checked with accepted values met Criterion (IV-1).

Table (IV-2a) is in reference to Criterion (IV-2a). Tables for Criterion (IV-2b) and Criterion (IV-3) are presented in Appendix D. The column labeled Relative Error gives the absolute value of the error given in Criterion (IV-2a). As evidenced by Table (IV-2a), the maximum relative error between the subroutine value and the accepted value is less than 10^{-3}. The additional tables presented in Appendix D also have maximum relative errors less than 10^{-3}. All the values produced by the subroutine that were checked with accepted values met Criterion (IV-1).

TABLE (IV-1a)

Bessel Function Subroutine Check

Against Published Standards for $J_{\nu+N}(k\rho)$

Range: $0.01 \leq k \leq 100$

$N = (0,1,2,\ldots,100)$

$\nu = 1/2$

$k\rho$	N	$J_{N+\frac{1}{2}}(k\rho)$ Subroutine	$J_{N+\frac{1}{2}}(k\rho)$ Standard*	Relative Error
.01	0	.0797871199	.0797871263	8.02(-8)
	1	.2659588395(-3)	.2659588606(-3)	7.93(-8)
	2	.5319191988(-6)	.5319192411(-6)	7.95(-8)
	12	.1009230707(-37)	.1009230776(-37)	6.84(-8)
.05	0	.1783380682	.1783380824	7.96(-8)
	1	.2972796639(-2)	.2972796874(-2)	7.91(-8)
	2	.2973009005(-4)	.2973009240(-4)	7.90(-8)
	12	.55092972289(-29)	.55092976611(-29)	6.75(-8)
0.1	0	.2518929203	.2518929403	7.94(-8)
	1	.8402033633(-2)	.8402034300(-2)	3.96(-8)
	2	.1680887056(-3)	.1680887190(-3)	7.97(-8)
	12	.3190882666(-25)	.3190882824(-25)	4.95(-8)
0.5	0	.5409737469	.5409737899	7.95(-8)
	1	.9170169233(-1)	.9170169960(-1)	7.93(-8)
	2	.9236407085(-2)	.9236407820(-2)	7.96(-8)
	12	.1734224713(-16)	.1734224842(-16)	7.44(-8)
1.0	0	.6713966538	.6713967071	7.94(-8)
	1	.2402978200	.2402978391	7.96(-8)
	2	.4949680629(-1)	.4949681022(-1)	7.94(-8)
	12	.9907033371(-13)	.9907034182(-13)	8.19(-8)
10	0	-.1372637248	-.1372637358	8.01(-8)
	10	.1630073534	.1630073664	7.98(-8)
50	0	-.2960583121(-1)	-.2960583189(-1)	2.30(-8)
	10	-.8484972142(-1)	-.8484972092(-1)	5.89(-9)
	100	.5749161075(-21)	.5749161043(-21)	5.57(-9)
100	0	-.4040213234(-1)	-.4040213272(-1)	9.41(-9)
	10	-.1561124543(-2)	-.1561123855(-2)	4.41(-7)
	100	.8681364822(-1)	.8681364620(-1)	2.33(-8)

*(Ref. 5)

Note: The number in parenthesis is the power of 10 by which the preceding number must be multiplied.

TABLE (IV-2a)

Fresnel Cosine Integral Check

of Subroutine Versus Published Standards

Range: $0.0014137 \leq k\rho \leq 100.53096$

$N = (0,2,4,\ldots,N_{max})$

$\nu = 1/2$

U	$k\rho = \frac{\pi}{2}U^2$	$\mathcal{C}(U)$-Subroutine (see Eq (76a)	$\mathcal{C}(U)$ Standard*	Relative Error
.03	.0014137	.0300000	.0300000	0.0
.04	.0025133	.0400000	.0400000	0.0
.06	.0056549	.0599997	.0599998	1.67(-6)
.08	.0100531	.0799986	.0799992	7.50(-6)
0.1	.015708	.0999959	.0999975	1.62(-5)
0.2	.0628319	.1998684	.1999211	2.64(-4)
0.5	.3926991	.4923317	.4923442	2.54(-5)
1.0	1.5707963	.7798923	.7798934	1.41(-6)
1.5	3.5342917	.4452353	.4452612	5.81(-5)
2.0	6.2831853	.4882271	.4882534	5.39(-5)
2.5	9.817477	.4574086	.4574130	5.62(-6)
3.0	14.137167	.6056911	.6057208	4.90(-5)
3.5	19.242255	.5325688	.5325724	6.76(-6)
4.0	25.132741	.4984154	.4984260	2.13(-5)
4.5	31.808626	.5260180	.5260259	1.50(-5)
5.0	39.269908	.5636193	.5636312	2.10(-5)
6.0	56.548668	.4995256	.4995315	1.24(-5)
6.5	66.366145	.4815931	.4816035	2.21(-5)
7.0	76.96902	.5454600	.5454671	1.35(-5)
7.5	88.357293	.5160098	.5160183	1.70(-5)
8.0	100.53096	.4997858	.4998022	3.33(-5)

*(Ref 5)

Note: The number in parenthesis is the power of 10 by which the preceding number must be multiplied.

Conclusions. Even though it is impossible to check for every possible value of $k\rho$, ν , and N due to the infinite number of values $k\rho$, ν , and N may be (though limited in range), the results just presented for the values of argument and order chosen all satisfy the criteria of this section. The values of argument and order were chosen so as to best exhibit the behavior (error-wise) of the subroutine for varied ranges of argument and order (and also on the availability of published standards). The final criterion that must be met is for the half-plane, presented in the next section.

Criterion and Results for Verifying the Half-Plane

The purpose of this section is to verify the use of a truncated version of Eqs (52) and (52') for the half-plane. By the similarity of Eqs (52) and (52') to Eqs (45) and (46) for the wedge, it is presumed that if the half-plane version can be verified, then the calculations for the highly conducting infinite wedge, presented in the next chapter, should have about the same order of percent error as the half-plane.

The solutions of Born and Wolf for the half-plane (see Chapter III) are used as the standard on which truncated versions of Eqs (52) and (52') are compared for relative error determination.

Criterion (IV-4). Use is made of Eqs (55) and (55') from Chapter III (Born and Wolf's classical half-plane solution), i.e.

$$\vec{J}_{s_{BW}} = -H_{\rho_s}\,\hat{a}_z$$

where $$H_{\rho_s} = E_o\sqrt{\frac{\epsilon_o}{\mu_o\pi}}\,e^{-i\left(k\rho-\frac{\pi}{4}\right)}\cdot\left\{i\sqrt{\frac{2}{k\rho}}\sin\left(\frac{\phi'}{2}\right) - 2\sin(\phi')\sqrt{\frac{\pi}{2}}\,e^{iu^2}\left[\frac{1}{2}-C(a)+i\left(S(a)-\frac{1}{2}\right)\right]\right\}$$

and where $$u = -\sqrt{2k\rho}\,\cos\left(\frac{\phi'}{2}\right)$$

$$a = \sqrt{\frac{2}{\pi}}\,u \qquad (55)$$

$$\left|\vec{J}\right|^2_{BW} = \vec{J}_{s_{BW}}\cdot\vec{J}^{*}_{s_{BW}} \qquad (55')$$

and the truncated version of Eqs (52) and (52')

$$\vec{J}_{s_H} = -H_{\rho_s}\,\hat{a}_z$$

where $$H_{\rho_s} = i\sqrt{\frac{\epsilon_o}{\mu_o}}\left(\frac{E_o}{k\rho}\right)\sum_{m=1}^{N_{max}}\left[i^{m/2}\cdot m\cdot J_{\frac{m}{2}}(k\rho)\cdot\sin\left(\frac{m\phi'}{2}\right)\right] \qquad (78)$$

$$\left|\vec{J}_S\right|^2_H = \vec{J}_{s_H}\cdot\vec{J}^{*}_{s_H} \qquad (78')$$

The case of the infinite half-volume (given by Eqs (57) and (58) of Chapter III) is given by a table in Appendix D, where Eq (57) is truncated in a similar manner as Eq (78).

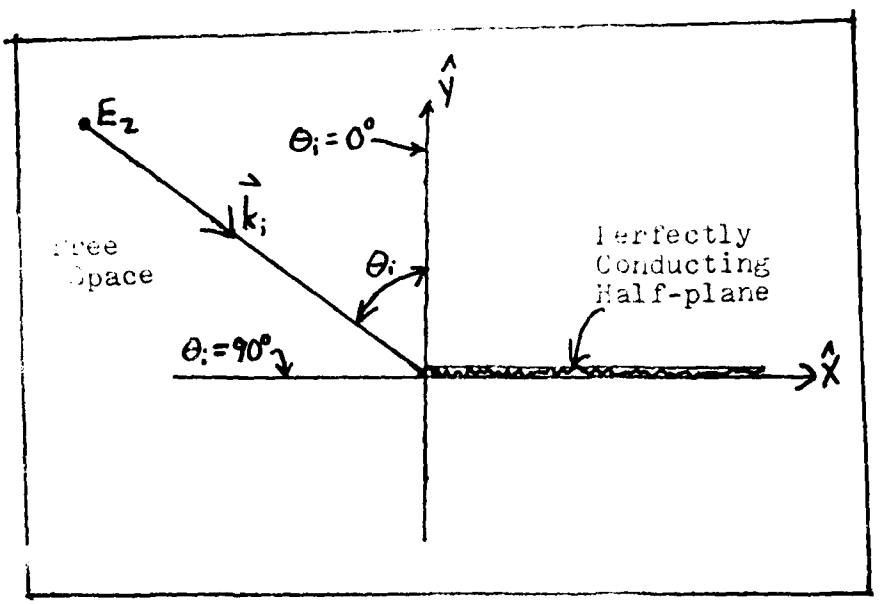

Figure 14. Half-plane geometry for Criterion (IV-4)

where the range of argument and order are given in Eq (75). N_{max} in this case, however, is equal to the integer portion of $m/2$ where the summation is truncated. It is then required that

$$\left| \frac{|\vec{J}_s|^2_{BW} - |\vec{J}_s|^2_H}{|\vec{J}_s|_{BW}} \right|$$

be less than 0.01 for excellent results and less than 0.05 for good results. Again, as before, the choices for 0.01 and 0.05 are completely arbitrary. The choice normally depends on the accuracy needed for a particular application or experiment.

The range of incident radiation angle, ϕ', is chosen so as to coincide with the range of angles of incidence, measured with respect to the surface normal, of the wedge presented in the next chapter.

Results. The following tables are results of computer runs to test Criterion (IV-4). The angle of incidence is now described by θ_i where θ_i is measured with respect to the surface normal (see Figure 14). Table (IV-4a) is for $\theta_i = 0^\circ$ (normal incidence) and Table (IV-4b) is for $\theta_i = 45^\circ$. Additional tables for θ_i are given in Appendix D. Without affecting the relative error, the quantity $\sqrt{\frac{\epsilon_o}{\mu_o}}\, E_o$ is normalized to equal one.

TABLE (IV-4a)

Half-Plane Check of Subroutine
Versus Born and Wolf's Solutions

Angle of Incidence: $\theta_i = 0^\circ$

Distance from Edge: $0.001 \leq k\rho \leq 100$

$k\rho$	$\vec{J}_s \cdot \vec{J}_s^*$ Subroutine†	$\vec{J}_s \cdot \vec{J}_s^*$ Born and Wolf†	Relative Error
.001	.3445668154(3)	.3445668614(3)	1.63(-7)
.002	.1780327007(3)	.1780327274(3)	1.50(-7)
.003	.1217155868(3)	.1217156048(3)	1.48(-7)
.004	.9324531437(2)	.9324532796(2)	1.46(-7)
.005	.7600434579(2)	.7600435669(2)	1.44(-7)
.006	.6441669591(2)	.6441670484(2)	1.39(-7)
.007	.5607918191(2)	.5607918942(2)	1.34(-7)
.008	.4978420458(2)	.4978421095(2)	1.28(-7)
.009	.4485782759(2)	.4485783299(2)	1.20(-7)
.01	.4089399381(2)	.4089399834(2)	1.11(-7)
.05	.1113554737(2)	.1113547673(2)	6.34(-6)
0.1	.7004508694(1)	.7004651448(1)	6.24(-5)
0.5	.3581315193(1)	.3581192719(1)	3.41(-5)
1.0	.3425171544(1)	.3425149724(1)	6.37(-6)
5.0	.4064911798(1)	.4064741893(1)	4.17(-5)
10	.4032786222(1)	.4032755312(1)	7.66(-6)
20	.3988001132(1)	.3987946918(1)	1.36(-5)
30	.4004309739(1)	.4004269284(1)	1.01(-5)
40	.3999589141(1)	.3999588194(1)	2.37(-7)
50	.3998500232(1)	.3998500575(1)	8.57(-8)
60	.4002128775(1)	.4002128661(1)	2.83(-8)
70	.3998080504(1)	.3998080486(1)	4.54(-9)
80	.4001249244(1)	.4001249246(1)	6.53(-10)
90	.3999562725(1)	.3999562692(1)	8.24(-9)
100	.3999732579(1)	.3999732559(1)	5.19(-9)

Note: Number in parenthesis is the power of 10 by which the number must be multiplied.

† Normalized for $\sqrt{\frac{\epsilon_o}{\mu_o}}\, E_o = 1$.

TABLE (IV-4b)

Half-Plane Check of Subroutine
Versus Born and Wolf's Solutions

Angle of Incidence: $\theta_i = 45^\circ$

Distance from Edge: $0.001 \leq k\rho \leq 100$

k	$\vec{J}_s \cdot \vec{J}_s^*$ Subroutine†	$\vec{J}_s \cdot \vec{J}_s^*$ Born and Wolf†	Relative Error
.001	.5672064751(3)	.5672065603(3)	1.50(-7)
.002	.2886873766(3)	.2886874211(3)	1.54(-7)
.003	.1951000809(3)	.1951001107(3)	1.53(-7)
.004	.1480164777(3)	.1480165002(3)	1.52(-7)
.005	.1196182206(3)	.1196182386(3)	1.51(-7)
.006	.1005984697(3)	.1005984848(3)	1.50(-7)
.007	.8695610556(2)	.8695611858(2)	1.50(-7)
.008	.7668500398(2)	.7668501540(2)	1.49(-7)
.009	.6866782750(2)	.6866783768(2)	1.48(-7)
.01	.6223260214(2)	.6223261132(2)	1.48(-7)
.05	.1471591210(2)	.1471591248(2)	2.58(-8)
0.1	.8339781086(1)	.8339773058(1)	9.62(-7)
0.5	.2816598597(1)	.2816001727(1)	2.12(-4)
1.0	.2068285593(1)	.2068281692(1)	2.37(-6)
5.0	.1784461110(1)	.1784323115(1)	7.73(-5)
10	.2019055026(1)	.2019047014(1)	4.46(-6)
20	.1995248743(1)	.1995224135(1)	1.23(-5)
30	.1999774545(1)	.1999747669(1)	1.34(-5)
40	.2002617145(1)	.2002596108(1)	1.05(-5)
50	.1996340769(1)	.1996326280(1)	7.25(-6)
60	.2004134840(1)	.2004125591(1)	4.61(-6)
70	.1995775856(1)	.1995723727(1)	2.61(-5)
80	.2004112916(1)	.2004083762(1)	1.45(-5)
90	.1996154167(1)	.1996138054(1)	8.07(-6)
100	.2003493654(1)	.2003429850(1)	3.18(-5)

† Normalized for $\sqrt{\frac{\epsilon_0}{\mu_0}}\, E_0 = 1$.

Note: The number in parenthesis is the power of 10 by which the preceding number must be multiplied.

Conclusions. All of the results obtained were excellent (< 0.01 relative error in accordance with Criterion (IV-4)). In addition to the tables shown in this chapter and Appendix D, checks were made for varying θ_i by 0.1 radians ($0 \leq \theta_i \leq \frac{\pi}{2}$) with the same results of "excellent." The results for the infinite half-volume, given in Appendix D, also came out as excellent.

Since Eqs (45) and (46) for the infinite wedge are similar in nature to Eqs (52) and (52') for the half-plane, then great promise is given to the success of a similar truncation working on the wedge equations.

V. Numerical Results for Wedge and Analysis

This chapter gives numerical results, presented in the form of graphs and tables, for the time-averaged power density as given by Eq (46) and by Eq (49) into Eq (18). The wedge to be considered is shown in Figure 15. It occupies the space (given in cylindrical coordinates) : $0 \leq \rho < \infty$, $-\pi/4 \leq \phi \leq \pi/4$, $-\infty < z < \infty$. The wedge is further assumed to be of finite conductivity σ ($\sigma \gg \omega\epsilon$) and imbedded in free space.

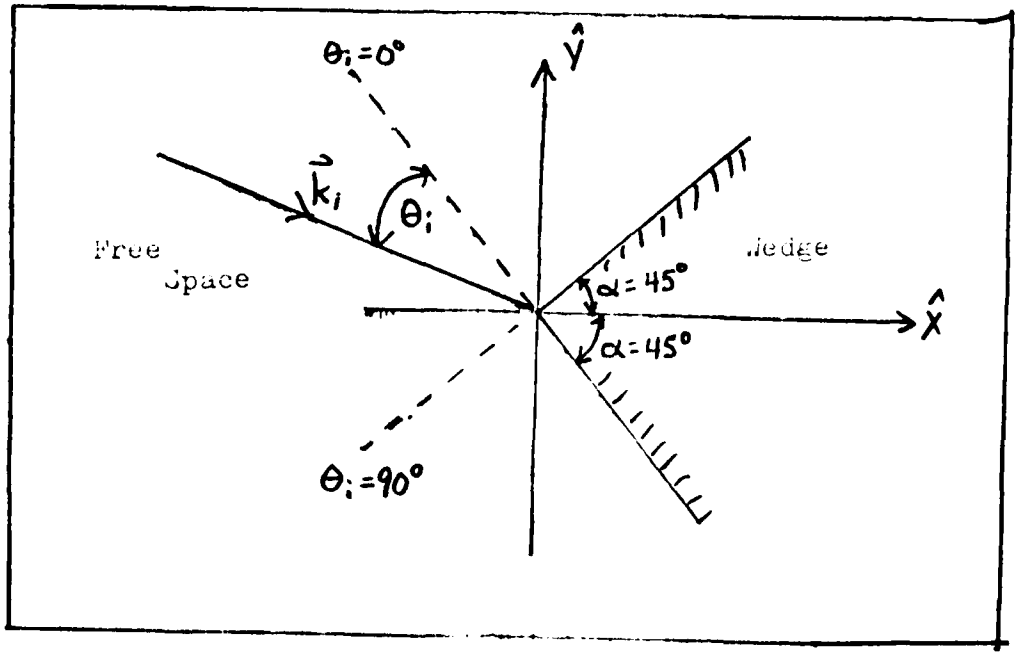

Figure 15. Wedge geometry considered for calculations

For computational reasons, the infinite summations given in Eqs (46) and (49) are truncated in the manner of the half-plane case verified in Chapter IV. The range of angles of the incident monochromatic plane wave is chosen as $0^\circ \leq \theta_i \leq 90^\circ$ (where θ_i is measured as shown in Figure 15). This range is chosen because it provides the worst case (higher power density loss) for the top wedge surface ($\phi = \frac{\pi}{4}$) near the vicinity of the edge. Thus, the range of incident angles for the incident radiation covers normal incidence ($\theta_i = 0^\circ$) to grazing incidence ($\theta_i = 90^\circ$). The range of distance from the wedge edge times the propagation constant k is $.001 \leq k\rho \leq 100$.

The following graphs yield the normalized ($\left[\frac{\epsilon_o E_o^2}{\sigma \delta \mu_o}\right] = 1$) time-averaged power density loss (in watts per square meter) for both TE and TM polarization of the incident field. Multiplication of the normalized power density loss by $\epsilon_o E_o^2 / \sigma \delta \mu_o$ for a given σ, δ, and E_o thus yields a first approximation to the watts per square meter absorbed by the wedge near the vicinity of the edge. The condition $\sigma >> \omega\epsilon$ is assumed satisfied. The graphs are of two types: (1) normalized power density loss versus $k\rho$ for various values of θ_i; (2) normalized power density loss versus θ_i for various values of $k\rho$.

The tables give the power density loss in terms of an absorption coefficient. The absorption coefficient, β, is the ratio of absorbed power density to the incident power density (irradiance); i.e. $\beta = \overline{\mathcal{P}}_{loss} / I_o$, where $\overline{\mathcal{P}}_{loss}$ is given

as in Eq (18) and I_o is the irradiance (in watts per square meter) and equal to $\sqrt{\frac{\epsilon_o}{\mu_o}} E_o^2$. Since the graphs yield $\bar{\mathcal{P}}_{loss}$ if the normalized power density is multiplied by $\epsilon_o E_o^2/\sigma\delta\mu_o$, then

$$\beta = \frac{\bar{\mathcal{P}}_{loss}}{I_o} = \frac{(\epsilon_o E_o^2/\sigma\delta\mu_o)\bar{\mathcal{P}}_{Norm}}{\sqrt{\epsilon_o/\mu_o}\, E_o^2}$$

$$= \frac{1}{\sigma\delta}\sqrt{\frac{\epsilon_o}{\mu_o}}\,\bar{\mathcal{P}}_{Norm} \qquad (79)$$

where $\bar{\mathcal{P}}_{Norm}$ is the normalized power density loss (as in the graphs). The results are for both TE and TM polarization of incident field wavelengths of 3.8 μm and 10.6 μm and wedge conductivity of $\sigma = 5.8 \times 10^7$ mhos/meter. The column labeled $\theta_i|_{max}$ gives the value of θ_i such that β is maximum at a given value of $k\rho$. The column labeled ρ (Å) gives the distance from the wedge edge in angstroms. This value depends on the incident field wavelength ($k = 2\pi/\lambda$).

The graphs and tables are now presented. Analysis of the results follows the graphs and tables.

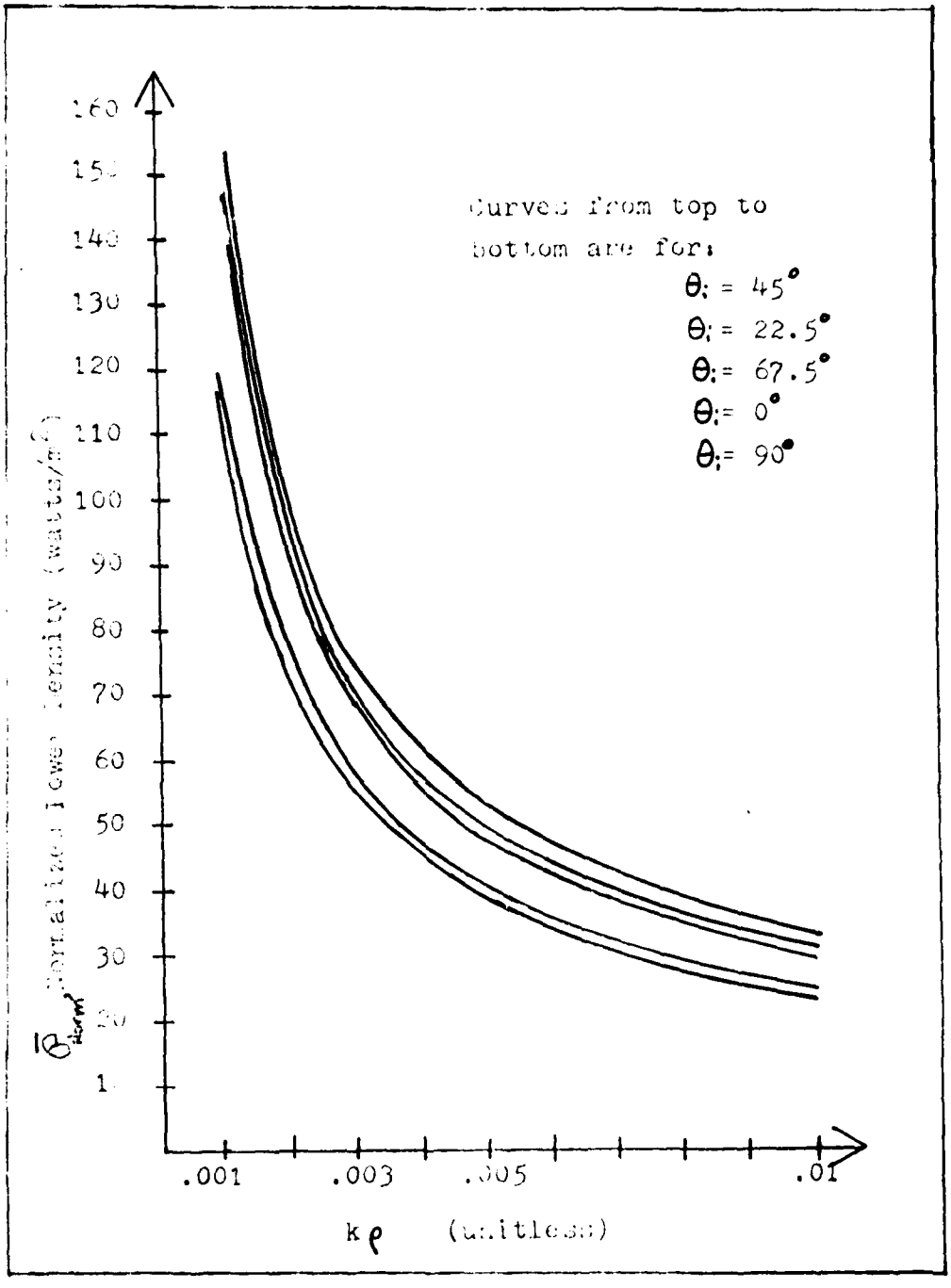

Figure 16. Normalized Power Density vs. $k\rho$, E.

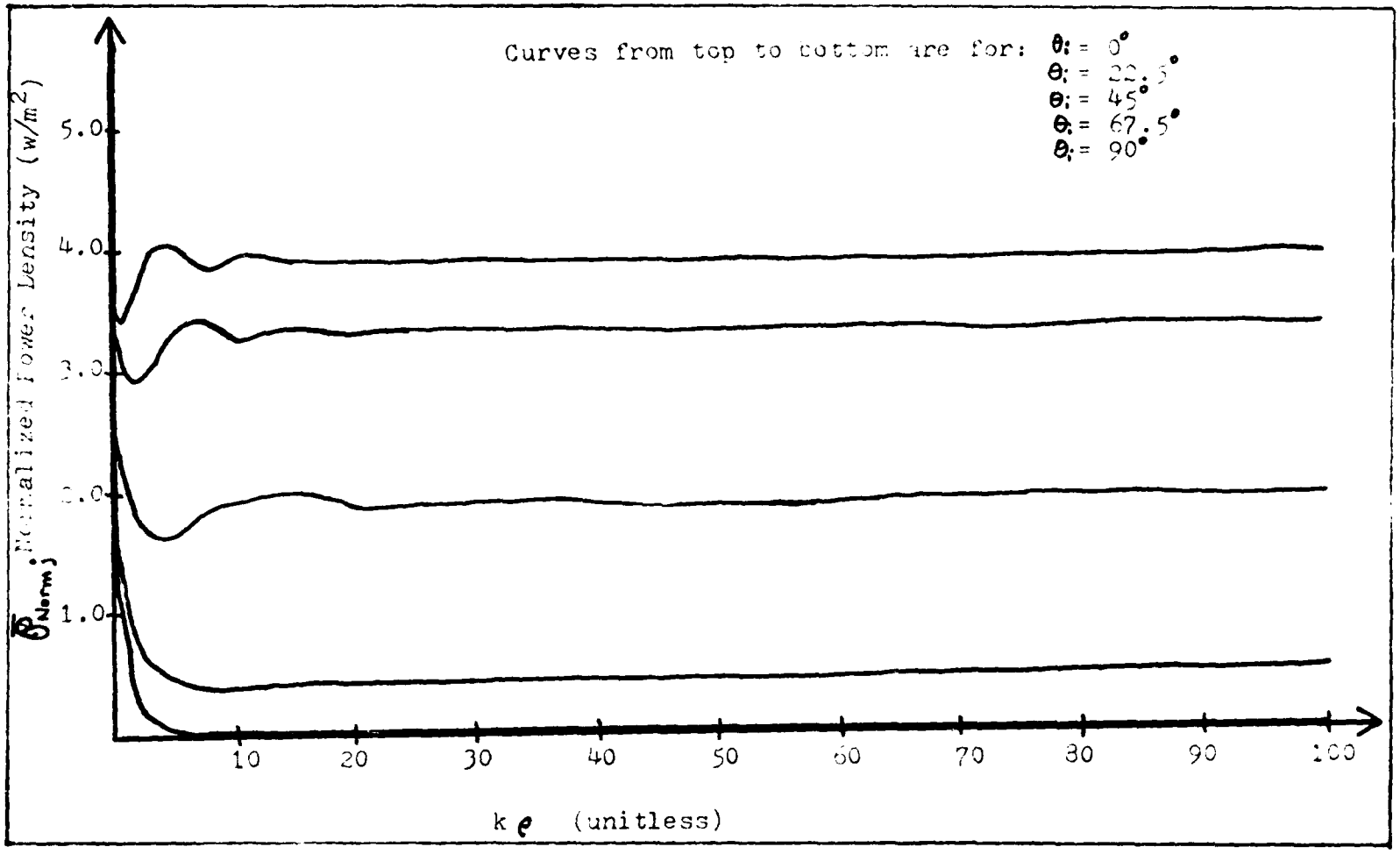

Figure 17. Normalized Power Density Vs. kρ , TM

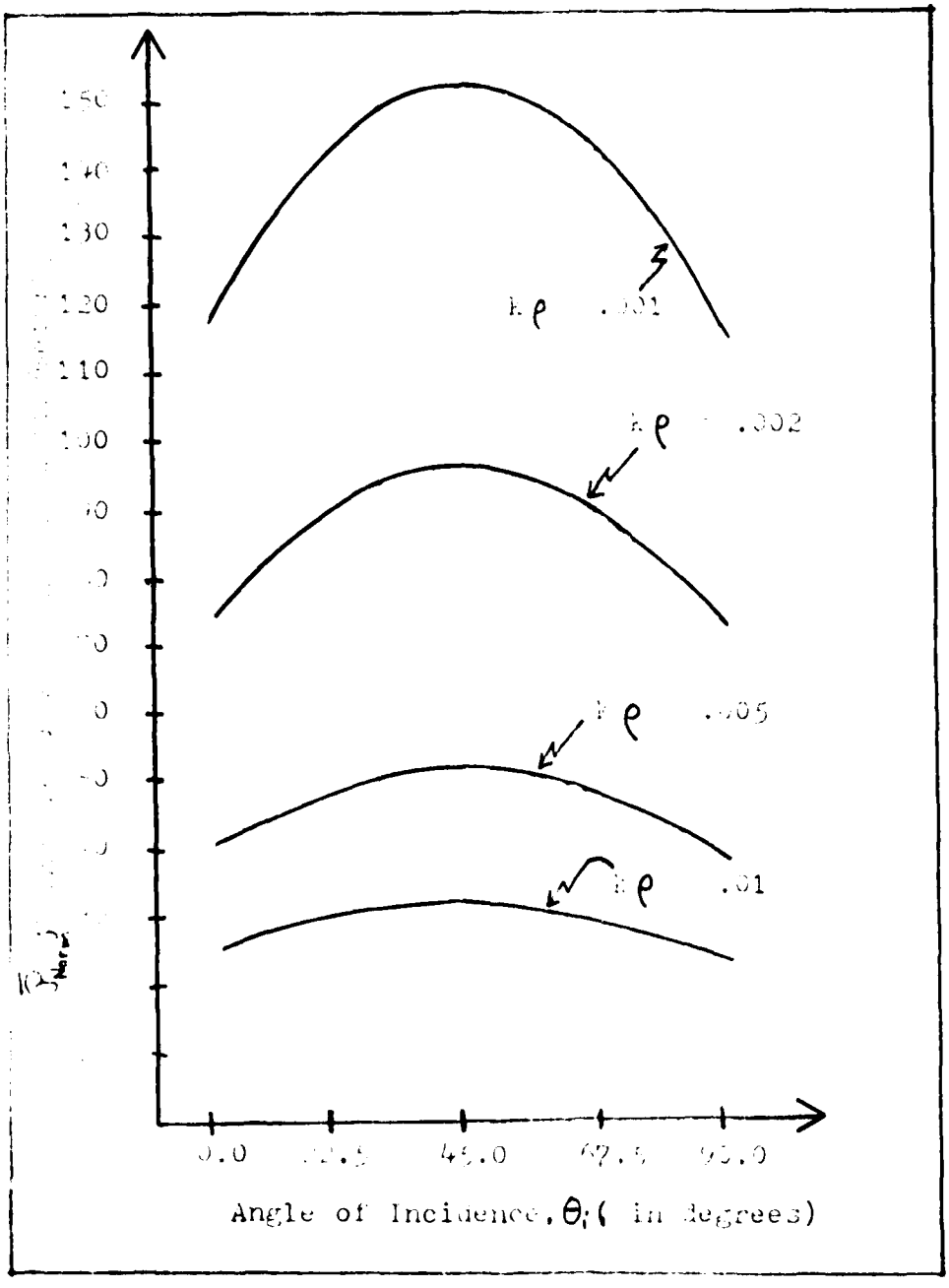

Figure 18. Normalized Power Density Vs. θ_i, TE

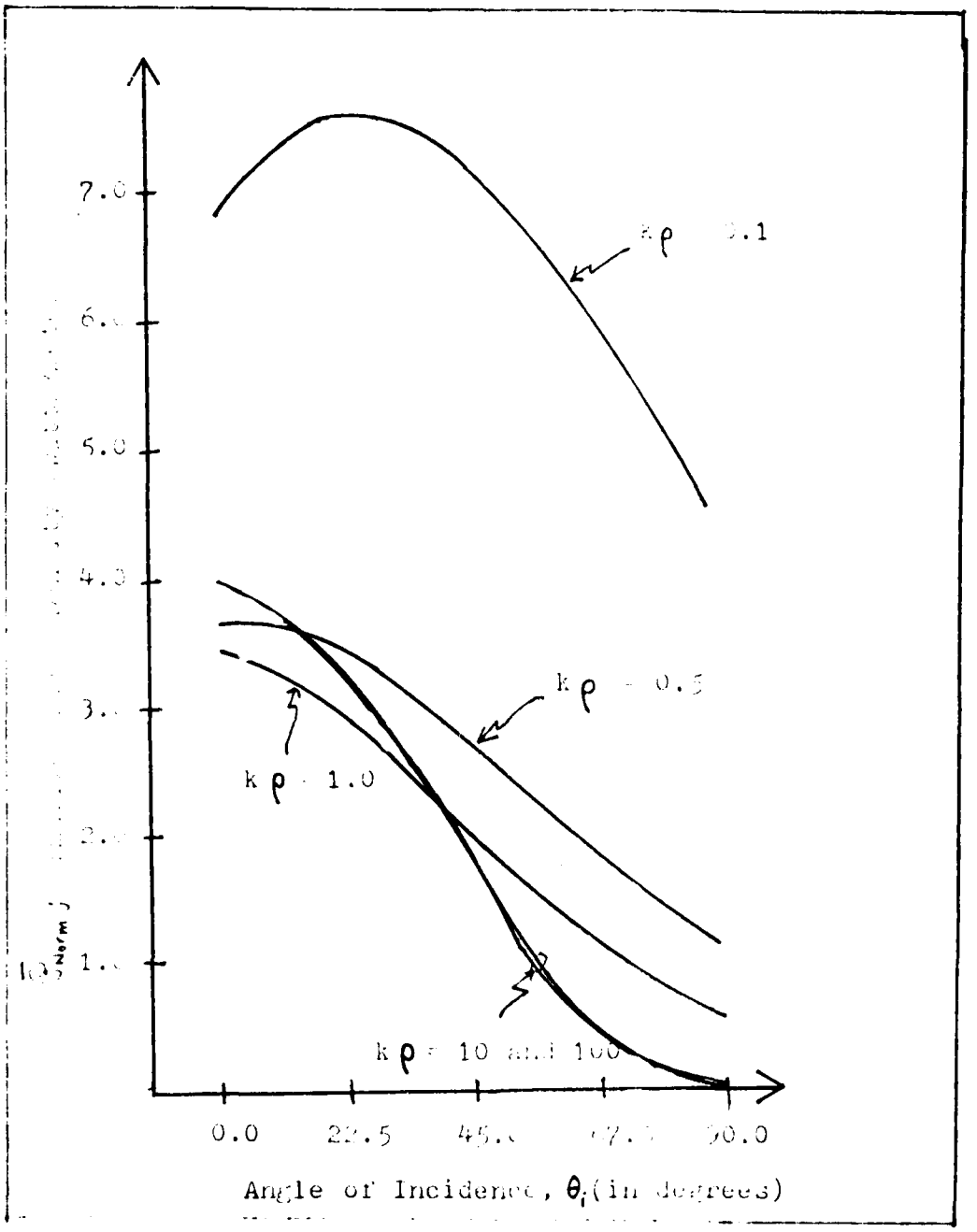

Figure 19. Normalized Power Density Vs. θ_i, TM

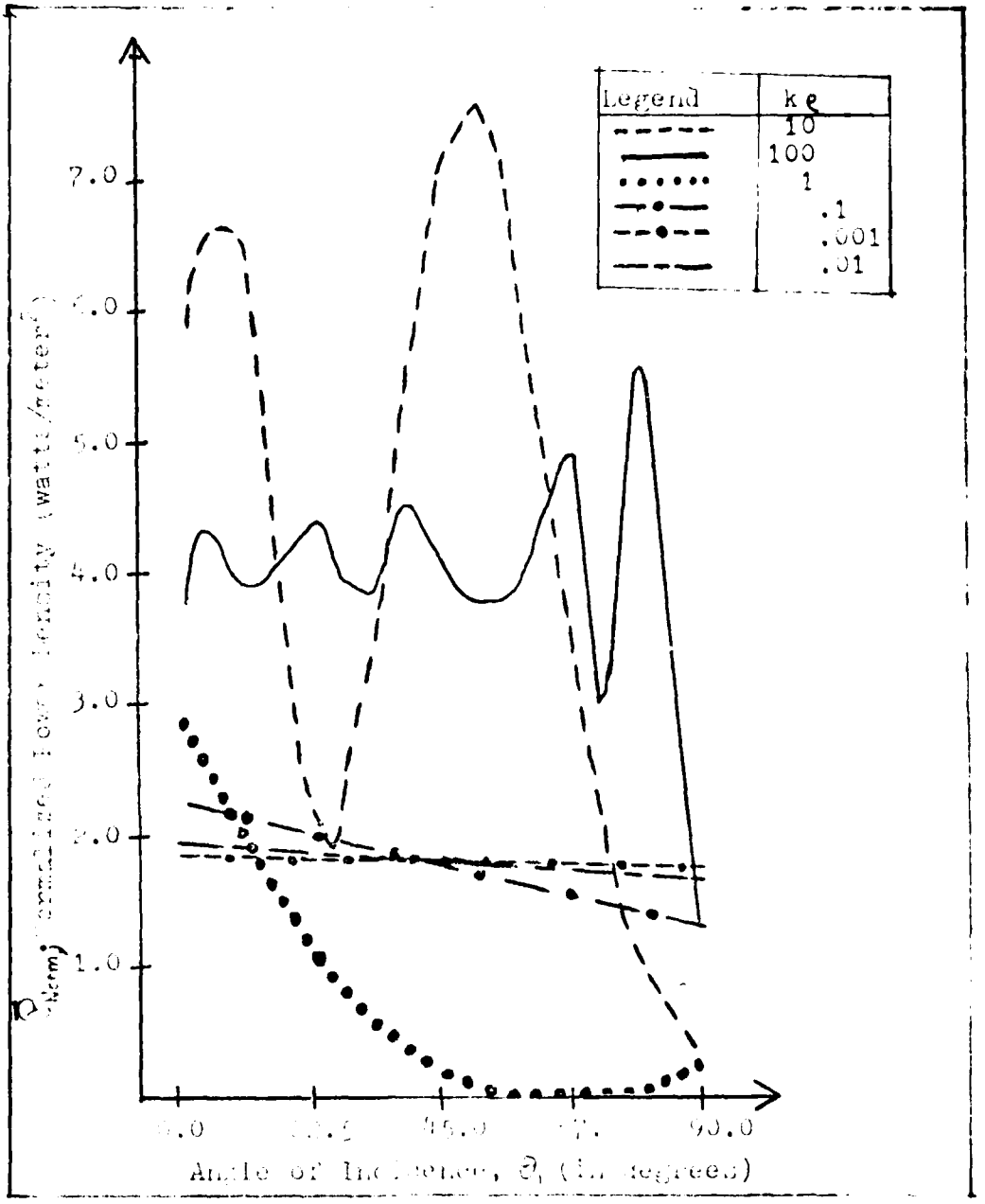

Figure 20. Normalized Power Density Vs. θ_i ,...

Figure 21. Normalized Power Density vs. x ρ for

Figure 22. Normalized Power Density vs. ρ, θ

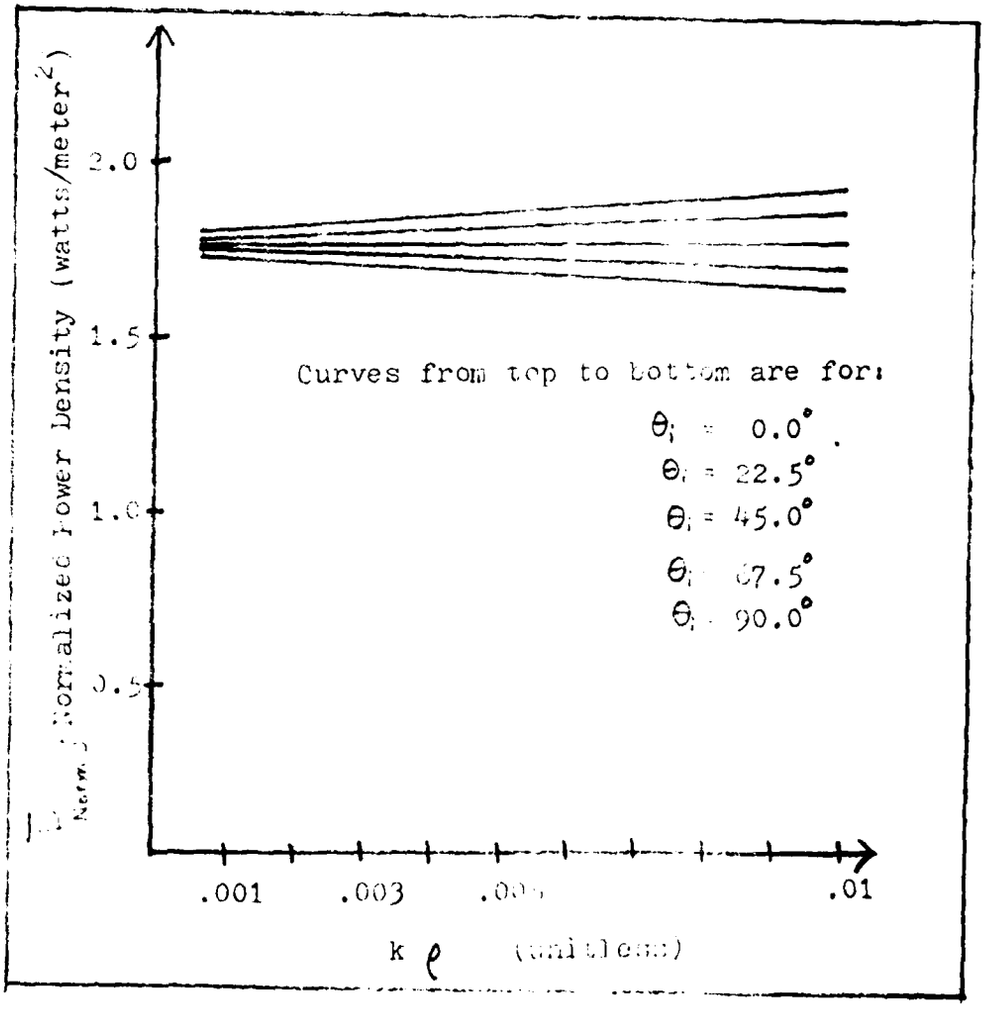

Figure 23. Normalized Power Density Vs. k ρ , TE

TABLE (V-1)

Absorption Coefficient for Wedge

Incident Wavelength: $\lambda_o = 3.8\,\mu m$

Skin Depth: $\delta = 74.4$ Å

$k\rho$	ρ (Å)	TE		TM	
		$\theta_i\|_{max}$	$\beta^\dagger$	$\theta_i\|_{max}$	$\beta^\dagger$
0.001	6.0479	0.0°	0.01107	45.0°	0.94672
0.005	30.239	0.0°	0.01132	45.0°	0.32390
0.01	60.479	0.0°	0.01155	45.0°	0.20418
0.05	302.39	0.0°	0.01269	36.9°	0.07149
0.1	604.79	0.0°	0.01365	25.4°	0.04672
0.5	3023.9	0.0°	0.01696	8.2°	0.02283
1.0	6047.9	0.0°	0.01746	0.0°	0.02140
5.0	30239.	16.8°	0.03491	0.0°	0.02498
10.0	60479.	48.3°	0.04583	0.0°	0.02479
50.0	302394.	74.1°	0.03539	0.0°	0.02460
100.0	604789.	77.0°	0.03388	0.0°	0.02460

TE: $\beta_{max} = 0.05110$ at $\rho \simeq 24192.$ Å ($k\rho = 4.0$) and $\theta_i|_{max} = 22.5°$

TM: $\beta_{max} = 0.94672$ at $\rho \simeq 6.0479$ A ($k\rho = 0.001$) and $\theta_i|_{max} = 45°$

For $\rho \geq 100$ Å,

$\beta_{max} = 0.14523$ at $\rho \simeq 100.0$ Å ($k\rho = 0.016$ and $\theta_i|_{max} = 45.0°$

$^\dagger \beta_{loss} = \beta \cdot \sqrt{\frac{\epsilon_o}{\mu_o}} E_o^2$

TABLE (V-2)

Absorption Coefficient for Wedge

Incident Wavelength: $\lambda_o = 10.6\,\mu m$

Skin Depth: $\delta = 124.3$ Å

$k\rho$	ρ(Å)	TE		TM	
		$\theta_i\|_{max}$	$\beta^\dagger$	$\theta_i\|_{max}$	$\beta^\dagger$
0.001	16.870	0.0°	0.00663	45.0°	0.56686
0.005	84.352	0.0°	0.00678	45.0°	0.19394
0.01	168.70	0.0°	0.00691	45.0°	0.12226
0.05	843.52	0.0°	0.00760	36.9°	0.04280
0.1	1687.0	0.0°	0.00818	25.4°	0.02798
0.5	8435.2	0.0°	0.01016	8.2°	0.01367
1.0	16870.	0.0°	0.01046	0.0°	0.01281
5.0	84352.	16.8°	0.02090	0.0°	0.01496
10.0	168704.	48.3°	0.02744	0.0°	0.01485
50.0	843521.	74.1°	0.02119	0.0°	0.01473
100.0	1687042.	77.0°	0.02029	0.0°	0.01473

TE: $\beta_{max} = 0.03060$ at $\rho \simeq 67482.$ Å ($k\rho = 4.0$) and $\theta_i|_{max} = 22.5°$

TM: $\beta_{max} = 0.56686$ at $\rho \simeq 16.870$ Å ($k\rho = 0.001$) and $\theta_i|_{max} = 45.0°$

For $\rho \geq 100$ Å,

$\beta_{max} = 0.17273$ at $\rho \simeq 100.$ Å ($k\rho = 0.006$) and $\theta_i|_{max} = 45.0°$

† $\bar{Q}_{loss} = \beta \cdot \sqrt{\frac{\epsilon_o}{\mu_o}} E_o^2$

Several observations are evident from the graphs just presented. Figure 16 through and including Figure 19 are are for the incident field having TM polarization (the electric field $\hat{z}$-polarized). Figure 20 through and including Figure 23 are for the incident field having TE polarization (the magnetic field $\hat{z}$-polarized).

Figure 16 plots $\overline{\sigma}_{Norm}$ versus $k\rho$ for the range of $0.001 \leq k\rho \leq 0.01$. The five curves are for different values of θ_i as indicated on the graph. It is evident that the maximum values of $\overline{\sigma}_{Norm}$ for each θ_i = constant curve occur closest to the edge at $k\rho = 0.0\rho1$. The maximum value of curs for $\theta_i = 45^\circ$ and $k\rho = 0.001$. It is also evident that the minimum values of $\overline{\sigma}_{Norm}$ occur for $\theta_i = 0^\circ$ (normal incidence) and $\theta_i = 90^\circ$ (grazing incidence). Figure 18, which plots $\overline{\sigma}_{Norm}$ versus θ_i for different values of $k\rho$ $(0.001 \leq k\rho \leq 0.01)$, shows that for each $k\rho$ = constant curve, $\overline{\sigma}_{Norm}$ is maximum at $\theta_i = 45^\circ$ and minimum at $\theta_i = 0^\circ$ and $\theta_i = 90^\circ$. All of the curves are nonlinear. This is to be expected for TM polarization, since for $\theta_i = 45^\circ$ (wedge angle $= 2\alpha = 90^\circ$), the surface current parallel to the edge will increase as $\rho^{-1/3}$ as the edge is approached (Ref 3: 19).

In direct contrast to the TM case for the range $0.001 \leq k\rho \leq 0.01$, is the TE case for the same range of $k\rho$. Figure 23 plots $\overline{\sigma}_{Norm}$ versus $k\rho$ $(0.001 \leq k\rho \leq 0.01)$. For $\theta_i = 0^\circ$ and $\theta_i = 22.5^\circ$, $\overline{\sigma}_{Norm}$ increases linearly with $k\rho$.

For $\theta_i = 67.5^\circ$ and $\theta_i = 90^\circ$, $\overline{\sigma}_{Norm}$ decreases linearly with $k\rho$. For $\theta_i = 45^\circ$, $\overline{\sigma}_{Norm}$ essentially remains constant for increasing $k\rho$. The value of $\overline{\sigma}_{Norm}$ is also much smaller (by around 20 to 80 times) than $\overline{\sigma}_{Norm}$ for the TM case, as in Figure 16. This is to be expected, however, because $\overline{\sigma}_{Norm}$ in the TM case is proportional to $(k\rho)^{-2}$ while $\overline{\sigma}_{Norm}$ in the TE case is not. Thus, very small values of $k\rho$ in the TM case ($k\rho << 1$) dramatically increases $\overline{\sigma}_{Norm}$. As evidenced from Figures 20 and 23 for the range $0.001 \leq k\rho \leq 0.01$ and $0^\circ \leq \theta_i \leq 90^\circ$, $\overline{\sigma}_{Norm}$ doesn't change as dramatically for the TE case as for the TM case in Figures 16 and 18.

Figure 17 shows that $\overline{\sigma}_{Norm}$ decreases rapidly from $k\rho < 0.5$ to $k\rho > 0.5$, and after the 'overshoot' present around $1 < k\rho < 5$ damps out, $\overline{\sigma}_{Norm}$ remains essentially constant for $k\rho > 10$. This constant value for $\overline{\sigma}_{Norm}$ decreases with increasing θ_i. This is to be expected since the reflectance, which is proportional to the reflected field flux over the incident field flux, increases with increasing angle of incidence.

Figures 21 and 22 plot $\overline{\sigma}_{Norm}$ versus $k\rho$ ($0.5 \leq k\rho \leq 100$) for various values of θ_i for TE polarization. In direct contrast to the TM case for this range of $k\rho$, $\overline{\sigma}_{Norm}$ does not damp out rapidly and approach a constant. Figure 21 shows that for $\theta_i = 0^\circ$ and $\theta_i = 45^\circ$, $\overline{\sigma}_{Norm}$ oscillates like a sinusoidal function times a decaying exponential function. Figure 22

shows similar behavior for $\theta_i = 22.5^\circ$, 67.5°, and 90°. The maximum values of $\bar{\sigma}_{Norm}$ occur for $\theta_i = 22.5^\circ$ and $k\rho \simeq 5$. The minimum values of $\bar{\sigma}_{Norm}$ occur for $\theta_i = 90^\circ$. Figures 21 and 22 for the TE case appear to oscillate about $\bar{\sigma}_{Norm}$ equal to four (except for $\theta_i = 90^\circ$), whereas in the TM case, $\bar{\sigma}_{Norm}$ decreases with θ_i for $k\rho > 1$. This is to be expected because the reflectance in the TM case changes less dramatically for increasing θ_i (until θ_i approaches 90°) than for the TE case (Ref 9: 80-89).

Figure 19 plots $\bar{\sigma}_{Norm}$ versus θ_i for various values of $k\rho$ ($0.1 \leq k \leq 100$). In relation to Figure 18, the values of $\bar{\sigma}_{Norm}$ is greatly reduced. Also, except for $k\rho = 0.1$, the various $k\rho$ = constant curves tend to lose the bell shape evident in the curves for $k\rho \leq 0.01$ in Figure 18. For $k\rho > 10$, the curves are nearly the same (as evidenced by the $k\rho$ =10 curve being almost the same as the $k\rho$ = 100 curve in Figure 19). This trend was evident from the data obtained for any value of $k\rho$ in this range. The TE case is again much different for the same range of $k\rho$. The various curves for $0.1 \leq k\rho \leq 100$ in Figure 20 do not share a common shape as the curves in Figure 19 for the TM case do. The highest values of $\bar{\sigma}_{Norm}$ appear on the $k\rho$ = 10 curve.

Figures 16 and 19 can be compared to similar plots for the half-plane (see Figures 24 and 25 in Appendix D). From such a comparison, it is evident that for the range of $k\rho$

closest to the edge ($0.001 \leq k\rho \leq 0.01$), the induced current in the half-plane is considerably higher than for the 90° wedge. This is expected since for the half-plane, the surface current parallel to the edge increases as $\rho^{-1/2}$ as the edge is approached. For the wedge, the surface current increases as $\rho^{-1/3}$ (Ref 3: 19). For distances further from the edge, however, $\overline{\Theta}_{Norm}$ for the wedge are on the order of $\overline{\Theta}_{Norm}$ for the half-plane. This indicates that the wedge reduces to the half-plane problem for $k\rho$ far enough away from the edge. This is true for both the TE and TM cases.

Tables (V-1) and (V-2) specialize the results for material parameters σ, ϵ, and μ and incident wavelength, λ_o. The skin depth, δ, is determined as in Eq (12). As given in Eq (79), the tables give the maximum absorption of incident flux (watts/meter^2) for a given distance from the wedge edge, ρ, and $\theta_i|_{max}$. Thus, the tables are in answer to the main objective of this thesis described in Chapter I.

Table (V-1) is for the incident field wavelength equal to 3. μm. With a conductivity σ assumed to be equal to x10^7 mhos/meter, the skin depth δ is thus equal to 7..4 Å (see Eq (15)). The maximum absorption of incident field flux is for a maximum value of β. For TE incident polarization, β_{max} occurs for a distance $\rho \simeq 24192.$ Å from the edge and $\theta_i|_{max} \simeq 22.5°$. The amount of time-averaged power density absorbed is thus equal to approximately five percent

of the incident field flux (in watts per square meter). Thus, for an incident field flux (TE polarized, θ_i=22.5°, λ_o= 3.8μm) of 10^6 watts/cm^2, the copper wedge would have to be able to absorb 5×10^4 watts/cm^2, otherwise it might be damaged a distance 2.4μm away from the edge. For an incident field of wavelength 10.6μm, Table (V-2) reveals the most absorption takes place at $\rho \simeq 6.7\mu$m and $\theta_i = 22.5°$ ($\beta \simeq 0.03$). These percentages are a percent or two higher than for copper of any geometrical shape for the 3.8μm to 10.6μm range of incident field wavelength (Ref 9: 88).

The TM case is much different. Tables (V-1) and (V-2) show β as high as 0.94672. This means that almost 95 percent of the incident field flux is absorbed at $k\rho = 0.001$ and $\theta_i = 0°$. The β calculated is only a first approximation, however. It is based on the assumption that the wedge is a linear, isotropic medium. For $k\rho = 0.001$, the distance from the edge is only about 16.9 Å for λ_o= 10.6μm and 6.0 Å for λ_o = 3.8μm. Since copper has a radius of about one angstrom, the linear assumption surely breaks down at $k\rho = 0.001$. This problem is not evident in the TE case because β_{max} occurs for a distance from the edge thousands of copper atoms away, hence accepting linearity of the medium as a valid assumption. It is now assumed that the linear

assumption be valid for $\rho \geq 100$ Å . The value of 100 Å is arbitrary, but necessary in order to establish a valid interpretation of the results. Thus, for $\rho \simeq 100$ Å , $k\rho$ must be greater than 0.006 for $\lambda_o = 10.6\ \mu m$ and $k\rho$ must be greater than .0165 for $\lambda_o = 3.8\ \mu m$. As evidenced from Figures 16 and 17, the maximum β will thus occur at $k\rho = 0.006$ ($\rho \simeq$ 100 Å) at $\lambda_o = 10.6\ \mu m$ and $\theta_i = 45°$, and at $k\rho = .0165$ ($\rho \simeq$ 100 Å) at $\lambda_o = 3.8\ \mu m$ and $\theta_i = 45°$. For $\lambda_o = 3.8\ \mu m$, β_{max} is about 0.14, which is much more than β_{max} for TE polarization. For $\lambda_o = 10.6\ \mu m$, however , the value of β_{max} implies that more than 17 percent of the incident flux is absorbed. For very large values of incident flux, damage to the wedge surface 100 Å from the edge would be more likely for the TM case than for the TE case.

The analysis given above for the graphs and tables are only a first approximation. The assumptions made included treating the wedge medium as linear and isotropic, using the surface current density for a perfect conductor ($\sigma \to \infty$), and the skin depth approximation. It is also assumed that all of the power density absorbed is convertible to heat (in watts per square meter). Another assumption made is that the infinite wedge solution can be used to approximate a finite wedge near the vicinity of the edge. Of note here is that for $k\rho$ large (greater that 10) , the effects of the edge on the induced surface current is dramatically reduced for either TM or TE polarization.

VI. Conclusions and Recommendations

The basic theory to solve the wave equation for given geometries has been investigated in this report. This theory has been applied to solve for the time-averaged power density dissipated on the surface of a highly conductive 90° infinite wedge illuminated by a monochromatic plane wave. By multiplying the normalized results by a constant depending on the material parameters of the wedge (σ, ϵ , μ) and the incident wave's frequency, numerical results are derived for a conducting surface of $\sigma = 5.8 \times 10^{7}$ mhos/meter and incident wavelengths of $\lambda_o = 3.8\mu m$ and $\lambda_o = 10.6\mu m$. Though the wedge used in the calculation is assumed infinite in extent, the effects of the edge on the induced surface current is seen to be dramatically reduced just a few wavelengths away from the edge.

This study has shown that for the electric field of a monochromatic plane wave polarized parallel to the sharp edge of a highly conductive 90° wedge, a high percentage (17 percent) of the incident flux can be absorbed 100 Å away from the edge. Though many assumptions are made to arrive at this result, it has been shown that it is a good first approximation. Therefore, this study provides a keener insight into the amount of incident flux absorbed by a highly conductive 90° wedge near the vicinity of the edge for both TE and TM polarization and various angles of incidence.

Since the results are only a first approximation, it is recommended that more factors be taken into account for more accurate results. These include thermal conductivity of the wedge as well as applying Fourier transform techniques for a finite wedge. More study into finding the difference in magnitude of the surface currents induced on the surface of a finite conductive wedge as opposed to one of infinite conductivity, is also recommended.

This study also opens the door to the need for better Bessel function routines to calculate high fractional order and high argument Bessel functions of the first kind, as evidenced by the shortcomings of the Bessel function subroutine discussed in Appendix C.

It is finally recommended that more study be given to solving for the eigenvalues and eigenfunctions for the type of problem encountered with the cone and parabolic cylinder. This is important because of the increase in use of such components as maxicons and reflexicons.

AD-A094 401 AIR FORCE INST OF TECH WRIGHT-PATTERSON AFB OH SCHOO--ETC F/G 20/13
INVESTIGATION OF LASER HEATING IN COMPONENTS WITH SHARP EDGES.(U)
DEC 80 J F BERKE

UNCLASSIFIED AFIT/GEO/PH/80-3 NL

2 OF 2
AD A094401

END
DATE FILMED
2-81
DTIC

Bibliography

1. Harrington, Roger F. Time Harmonic Electromagnetic Fields. New York: McGraw-Hill Book Co., 1961.

2. Spiegel, Murray R. Schaum's Outline of Theory and Problems of Advanced Mathematics for Engineers and Scientists. New York: McGraw-Hill Book Co., 1971.

3. Collin, Robert E. and Francis J. Zucker. Antenna Theory, Part 1. New York: McGraw-Hill Book Co., 1969.

4. Weast, Robert C. Handbook of Chemistry and Physics (52nd Edition). Cleveland: Chemical Rubber Co., 1971.

5. Abramowitz, Milton and Irene A. Stegun. Handbook of Mathematical Functions. Washington DC: National Bureau of Standards Applied Mathematics Series 55, 1965.

6. Born, Max and Emil Wolf. Principles of Optics. (Second Edition). New York: Macmillan Co., 1964.

7. Lebedev, N.N. and Richard A. Silverman. Special Functions and Their Applications. New York: Dover Publications, Inc., 1969.

8. Rogers, C.C., et al. "The Scattering of a Plane Electromagnetic Wave by a Finite Cone," International Series of Monographs on Electromagnetic Waves, Part 1, edited by E.C. Jordan. New York: Macmillan Co., 1963.

9. Hecht, Eugene and Alfred Zajac. Optics. Reading MA: Addison-Wesley Publishing Co., 1976.

10. Whitford, Les, Computer Expert. Personal interview. ASD Computer Center, Wright-Patterson AFB OH, 1980.

11. Goldstein, M. and R.M. Thaler. "Recurrance Techniques for Calculation of Bessel Functions," Mathematical Tables and Other Aids to Computation, 13: 102-108 (January 1959).

12. Goldstein, M. and R.M. Thaler. "Bessel Functions for Large Arguments," Mathematical Tables and Other Aids to Computation, 12: 18-26 (January 1958).

13. Computation Laboratory of the National Applied Mathematics Laboratories, National Bureau of Standards. Tables of Bessel Functions of Fractional Order, Volumn I. New York: Columbia University Press, 1948.

Bibliography (Cont'd)

14. Staff of the Computation Laboratory. Tables of the Bessel Functions of the First Kind of Orders, Zero to One Hundred Thirty Five, Volumes I thru XII. Cambridge MA: Harvard University Press, 1951.

15. Dente, Gregory C. "Polarization Effects in Resonators," Applied Optics, 18 (17): 2911 (September 1, 1979).

16. Lorrain, Paul and Dale R. Corson. Electromagnetic Fields and Waves. (Second Edition) San Francisco: W.H. Freeman and Co., 1970.

APPENDIX A

Definition of Certain Functions

The purpose of this Appendix is to lend support to various references made within this thesis to the definitions of certain functions.

Bessel Functions (Ref 1:460-464)

Bessel's equation of order ν is

$$x \frac{d}{dx}(x \frac{dy}{dx}) + (x^2 - v^2)y = 0 \qquad \text{(A-1)}$$

Solutions to Eq (A-1) include

$$J_v(x) = \sum_{m=0}^{\infty} \frac{(-1)^m (x)^{2m+v}}{m!\,(m+v)!\,(2)^{2m+v}} \qquad \text{(A-2)}$$

$$J_{-v}(x) = \sum_{m=0}^{\infty} \frac{(-1)^m (x)^{2m-v}}{m!\,(m-v)!\,(2)^{2m-v}} \qquad \text{(A-3)}$$

where $J_v(x)$ and $J_{-v}(x)$ are Bessel functions of the first kind of order v and -v, respectively. Bessel's function of the second kind of order v is also a solution to Eq (A-1) and is given by

$$N_v(x) = \frac{J_v(x)\cos(v\pi) - J_{-v}(x)}{\sin(v\pi)} \qquad \text{(A-4)}$$

Hankel functions of the first and second kind of order v are also solutions to Eq (A-1) and defined as

$$H_v^{(1)}(x) = J_v(x) + i\, N_v(x) \tag{A-5}$$

$$H_v^{(2)}(x) = J_v(x) - i\, N_v(x) \tag{A-6}$$

respectively.

Asymptotic approximations for Eqs (A-2) and (A-4) for $x \rightarrow 0$ are given by

$$J_v(x) \xrightarrow[x\to 0]{} \frac{1}{v!}\left(\frac{x}{2}\right)^v \tag{A-7}$$

$$N_v(x) \xrightarrow[x\to 0]{} -\frac{(v-1)!}{\pi}\left(\frac{2}{x}\right)^v \tag{A-8}$$

provided $\mathrm{Re}\{v\} > 0$. For large arguments $(x \longrightarrow \infty)$, the leading terms in the asymptotic expansion are given by

$$J_v(x) \xrightarrow[x\to\infty]{} \sqrt{\frac{2}{\pi x}}\cos\left(x - \frac{\pi}{4} - \frac{v\pi}{2}\right) \tag{A-9}$$

$$N_v(x) \xrightarrow[x\to\infty]{} \sqrt{\frac{2}{\pi x}}\sin\left(x - \frac{\pi}{4} - \frac{v\pi}{2}\right) \tag{A-10}$$

provided $|\text{phase } (x)| < \pi$. Equations (A-9) and (A-10) into Eqs (A-5) and (A-6) thus yield

$$H_\nu^{(1)}(x) \xrightarrow[x\to\infty]{} \sqrt{\frac{2}{i\pi x}}\; i^{-\nu} e^{ix} \tag{A-11}$$

$$H_\nu^{(2)}(x) \xrightarrow[x\to\infty]{} \sqrt{\frac{2i}{\pi x}}\; i^{\nu} e^{-ix} \tag{A-12}$$

Associated Legendre Functions (Ref 7:164, 193)

The associated Legendre equation is

$$(1 - z^2)\frac{d^2u}{dz^2} - 2z\frac{du}{dz} + \left[\nu(\nu+1) - \frac{m^2}{1-z^2}\right]u = 0 \tag{A-13}$$

for arbitrary ν and $m = (0,1,2,3,\ldots)$. Solutions to Eq (A-13) include

$$P_\nu^m(z) = (z^2 - 1)^{m/2}\;\frac{d^m P_\nu(z)}{dz^m} \tag{A-14}$$

where $P_\nu^m(z)$ is called the associated Legendre function of the first kind. $P_\nu(z)$ is a solution to Eq (A-14) for $m = 0$ and called Legendre's function of the first kind. It is given as

$$P_\nu(z) = \sum_{k=0}^{\infty} \frac{(-1)^k(\nu+k)!}{(m!)^2(\nu-m)!}\left(\frac{1-z}{2}\right)^k - \frac{\sin(\nu\pi)}{\pi}\sum_{k=N+1}^{\infty}\frac{(k-1-\nu)!\,(k+\nu)!}{(m!)^2}\left(\frac{1-z}{2}\right)^k \tag{A-15}$$

where N is the closest integer to ν such that $N \leq \nu$.

Hermite Functions (Ref 7:260, 284, 294)

The differential equation

$$\frac{d^2v}{dz^2} - 2z\frac{dv}{dz} + 2\nu v = 0 \qquad \text{(A-16)}$$

has Hermite functions for solutions. Hermite's function of degree is given by

$$H_\nu(z) = \frac{2^\nu \Gamma(\frac{1}{2})}{\Gamma(\frac{1-\nu}{2})} \Phi\left(-\frac{\nu}{2}, \frac{1}{2}; z^2\right) + \frac{2^\nu \Gamma(-\frac{1}{2})}{\Gamma(-\frac{\nu}{2})} z\, \Phi\left(\frac{1-\nu}{2}, \frac{3}{2}; z^2\right) \qquad \text{(A-17)}$$

where $\Phi(\alpha,\gamma;z)$ is known as the confluent hypergeometric function. It is given by

$$\Phi(\alpha,\gamma;z) = \sum_{k=0}^{\infty} \frac{(\alpha)_k z^k}{(\gamma)_k k!}$$

for $|z| < \infty$

and $\gamma \neq (0,-1,-2,-3,\ldots)$ (A-18)

For large values of argument $(z \longrightarrow \infty)$, then

$$H_{\nu}(z) \xrightarrow[z\to\infty]{} (2z)^{\nu} \tag{A-19}$$

$$H_{-\nu-1}(iz) \xrightarrow[z\to\infty]{} e^{-\frac{1}{2}(\nu+1)\pi i}(2z)^{-\nu-1} \tag{A-20}$$

For ν equal to an integer n, then the asymptotic expressions are approximated by

$$H_n(iz) \xrightarrow[z\to\infty]{} i^n(2z)^n \tag{A-21}$$

$$H_{-n-1}(z) \xrightarrow[z\to\infty]{} (2z)^{-n-1} \tag{A-22}$$

APPENDIX B

Miscellaneous Support of Thesis

The purpose of this Appendix is to lend support to various references made within this thesis.

Derivation of Source Current Density

The details leading to the derivation of Eq (36) is presented in this section. In reference to Figure 7a in Chapter III, the current filament is considered to be an impulse of current of strength I (in amps). Figure 7b represents a vanishingly small area surrounding the current filament; small enough so that the current filament can be considered as a current sheet ($\rho = \rho'$) separating the regions for $\rho > \rho'$ and $\rho < \rho'$.

Applying Ampère's circuital law (Ref 1:33)

$$\oint_{\text{Closed Path}} \vec{H} \cdot d\vec{l} = I^t \qquad \text{(B-1)}$$

where I^t is the total current on the surface of the boundary enclosed by the path shown in Figure 7b, then (Ref 1:34)

$$\hat{n} \times \left[\vec{H}_I - \vec{H}_{II}\right] = \vec{J}_s \qquad \text{(B-2)}$$

is obtained for the surface current density. It is noted that $\hat{n} = \hat{a}_\rho$ and $\vec{H}_I$ is the magnetic field on the Region I

side of the surface boundary and $\vec{H}_{II}$ is the magnetic field on the Region II side of the surface boundary. Both $\vec{H}_I$ and $\vec{H}_{II}$ must be $\hat{\phi}$-polarized because $\vec{J}_s$ is $\hat{z}$-polarized and $\hat{n} = \hat{a}_\rho$. Taking the Region I side of the boundary to be located at $\rho = \rho'+$ and the Region II side of the boundary to be located at $\rho = \rho'-$, then the scalar surface boundary equation is written as

$$J_z = H_\phi(\rho'+) - H_\phi(\rho'-) \tag{B-3}$$

where $H_\phi(\rho'+)$ represents the surface magnetic field in Region I and $H_\phi(\rho'-)$ represents the surface magnetic field in Region II. Recalling Eq (2')

$$\nabla \times \vec{E} = -i\omega\mu_o \vec{H} \tag{B-4}$$

and since $\vec{H}$ at the surface is $\hat{\phi}$-polarized and $\vec{E}$ is $\hat{z}$-polarized, Eq (2') is then written in scalar form as

$$\frac{\partial E_z}{\partial \rho} = -i\omega\mu_o H_\phi \tag{B-5}$$

Substitution of Eq (31) for E_z into the above equation yields

$$H_\phi = \begin{cases} -\frac{ik}{\omega\mu_o} \sum_v a_v H_v^{(2)}(k\rho') J_v'(k\rho) \sin[v(\phi'-\alpha)] \sin[v(\phi-\alpha)], & \rho < \rho' \\ -\frac{ik}{\omega\mu_o} \sum_v a_v J_v(k\rho') H_v^{(2)\prime}(k\rho) \sin[v(\phi'-\alpha)] \sin[v(\phi-\alpha)], & \rho > \rho' \end{cases} \quad \text{(B-6)}$$

where $J_v'(k\rho)$ denotes $\frac{\partial J_v(k\rho)}{\partial \rho}$ and $H_v^{(2)\prime}(k\rho)$ denotes $\frac{\partial H_v^{(2)}(k\rho)}{\partial \rho}$. Applying Eq (B-3) to Eq (B-6), with $\rho'+$ for $\rho > \rho'$ and $\rho'-$ for $\rho < \rho'$ and then setting $\rho = \rho'$, yields for the source

$$J_z = -\frac{ik}{\omega\mu_o} \sum_v a_v \sin[v(\phi'-\alpha)] \sin[v(\phi-\alpha)] \cdot [J_v(k\rho') H_v^{(2)\prime}(k\rho') - H_v^{(2)}(k\rho') J_v(k\rho')] \quad \text{(B-7)}$$

Using the relations (Ref 1:402)

$$\begin{aligned} H_v^{(2)}(x) &= J_v(x) - i\, N_v(x) \\ H_v^{(2)\prime}(x) &= J_v'(x) - i\, N_v'(x) \end{aligned} \quad \text{(B-8)}$$

where the primes denote the first derivative with respect to the variable x and $N_v(x)$ is the Bessel function of the second kind of order v, and then by applying the Wronskian of Bessel's equation given by (Ref 1:463)

$$J_\nu(x)\,N_\nu'(x) - N_\nu(x)\,J_\nu'(x) = \frac{2}{\pi x} \qquad \text{(B-9)}$$

implies that

$$\begin{aligned} J_\nu(k\rho')H_\nu^{(2)\prime}(k\rho) - H_\nu^{(2)}(k\rho')J_\nu'(k\rho') \\ &= J_\nu(k\rho')J_\nu'(k\rho') - iJ_\nu(k\rho')N_\nu'(k\rho') \\ &\quad - J_\nu(k\rho')J_\nu'(k\rho') + iN_\nu(k\rho')J_\nu'(k\rho') \\ &= -i\left[J_\nu(k\rho')N_\nu'(k\rho') - N_\nu(k\rho')J_\nu'(k\rho')\right] \\ &= -i\frac{2}{\pi k\rho'} \end{aligned} \qquad \text{(B-10)}$$

Substituting this result into the expression for J_z yields

$$J_z = -\frac{2}{\pi\omega\mu_0\rho'}\sum_\nu a_\nu \sin[\nu(\phi'-\alpha)]\sin[\nu(\phi-\alpha)] \qquad \text{(B-11)}$$

Leontovich Boundary Condition (Ref 3:18)

As long as the radius of curvature of a good conductor is much larger than the skin depth, the conductor boundary may be described by an impedance boundary condition, where ζ_s of Eq (17) is the surface impedance. Since the wedge has a flat top surface and the point of observation isn't on the edge singularity, the above stated Leontovich Boundary Condition is applicable.

Parabolic Cylinder

The purpose of this section is to derive Eqs (62), (63), and (64). Recalling Eqs (60) and (61),

$$\frac{1}{c^2(u^2+v^2)}\left(\frac{\partial^2\psi}{\partial u^2}+\frac{\partial^2\psi}{\partial v^2}\right)+\frac{\partial^2\psi}{\partial z^2}+k^2\psi=0 \qquad (60)$$

$$\psi(u,v,z)=U(u)\,V(v)\,Z(z) \qquad (61)$$

then the method of Separation of Variables can be used. Substitution of Eq (61) into Eq (60), dividing through by $\psi \neq 0$, and rearranging yields

$$\frac{1}{c^2(u^2+v^2)}\left(\frac{1}{U}\frac{\partial^2 U}{\partial u^2}+\frac{1}{V}\frac{\partial^2 V}{\partial v^2}\right)+k^2=-\frac{1}{Z}\frac{\partial^2 Z}{\partial z^2} \qquad (B\text{-}12)$$

The right side of Eq (B-12) is a function in z only, while the left side is a function in u and v. Therefore, in order for the above equation to be true for any u, v, and z, both sides must be equal to a constant. Denoting this constant by k_z^2 implies

$$-\frac{1}{Z}\frac{\partial^2 Z}{\partial z^2}=k_z^2 \qquad (B\text{-}13)$$

Substitution of Eq (B-13) into the previous equation, multiplying through by $c^2(u^2+v^2)$, and rearranging yields

$$\frac{1}{U}\frac{\partial^2 U}{\partial u^2} + c^2\left(k^2 - k_z^2\right)u^2 = -\frac{1}{V}\frac{\partial^2 V}{\partial v^2} - c^2\left(k^2 - k_z^2\right)v^2 \quad \text{(B-14)}$$

The right side of Eq (B-14) is a function in v only, and the left side is a function in u only. Therefore, both sides must be equal to a constant in order for the above equation to be true for any u and v. Denoting this constant by $2\mu + 1$, the left side of the above equation becomes

$$\frac{1}{U}\frac{\partial^2 U}{\partial u^2} + c^2\left(k^2 - k_z^2\right)u^2 = 2\mu + 1 \quad \text{(B-15)}$$

and the right side becomes

$$\frac{1}{V}\frac{\partial^2 V}{\partial v^2} + c^2\left(k^2 - k_z^2\right)v^2 = -(2\mu + 1) \quad \text{(B-16)}$$

Since Eqs (B-13), (B-15), and (B-16) are functions in only one variable, the partial derivatives are written as ordinary derivatives. Also, by multiplying Eqs (B-13), (B-15), and (B-16) through by Z, U, and V, respectively, and rearranging yields

$$\frac{d^2 Z}{dz^2} + k_z^2 Z = 0 \quad \text{(62)}$$

$$\frac{d^2 U}{du^2} + \left[(ck_D)^2 u^2 - (2\mu + 1)\right]U = 0 \quad \text{(B-17)}$$

$$\frac{d^2V}{dv^2} + \left[(ck_D)^2 v^2 + (2\mu+1)\right] V = 0 \qquad \text{(B-18)}$$

where k_D^2 is defined by

$$k^2 = k_D^2 + k_z^2 \qquad \text{(B-19)}$$

A substitution of variables is now performed so as to put Eqs (B-19) and (B-20) into the form

$$\frac{d^2 f(\zeta)}{d\zeta^2} + \left[\pm\left(\nu+\tfrac{1}{2}\right) - \frac{\zeta^2}{4}\right] f(\zeta) \qquad \text{(B-20)}$$

which has parabolic cylinder functions as solutions for and where the variable ζ and parameter ν are, in general, real or complex (Ref 7:284).

Examining Eq (B-17) first, the following substitution of variables are made:

Let $$\beta = \sqrt{2ik_Dc}\,u \qquad \text{(B-21)}$$

Then $$\beta^2 = 2ik_Dc\,u^2$$

Using the chain rule, then $$\frac{d}{du} = \frac{d\beta}{du}\frac{d}{d\beta} = \sqrt{2ik_Dc}\frac{d}{d\beta}$$

and $$\frac{d}{du^2} = \frac{d}{du}\left(\sqrt{2ik_Dc}\frac{d}{d\beta}\right) = 2ik_Dc\frac{d^2}{d\beta^2}$$

Making the above substitutions into Eq (B-17) yields

$$2ik_Dc\,\frac{d^2U\left(\frac{\beta}{\sqrt{2ik_Dc}}\right)}{d\beta^2}+\left[\frac{ck_D}{2i}\beta^2-(2\mu+1)\right]U=0$$

Dividing the above equation by $2ik_Dc$ ($\neq 0$) and defining

$$\nu+\frac{1}{2}=-\left(\frac{2\mu+1}{2ik_Dc}\right) \tag{B-22}$$

results in

$$\frac{d^2U\left(\frac{\beta}{\sqrt{2ik_Dc}}\right)}{d\beta^2}+\left[-\frac{\beta^2}{4}+\left(\nu+\frac{1}{2}\right)\right]U\left(\frac{\beta}{\sqrt{2ik_Dc}}\right)=0 \tag{B-23}$$

In a similar fashion, Eq (B-18) becomes

$$\frac{d^2V\left(\frac{\gamma}{\sqrt{2ik_Dc}}\right)}{d\gamma^2}+\left[-\frac{\gamma^2}{4}-\left(\nu+\frac{1}{2}\right)\right]V\left(\frac{\gamma}{\sqrt{2ik_Dc}}\right)=0 \tag{B-24}$$

where the substitution of variable

$$\gamma=\sqrt{2ik_Dc}\,v \tag{B-25}$$

was made along with Eq (B-22).

Using the substitutions

$$\begin{aligned}\beta&=\sqrt{2}\,u\\ \gamma&=\sqrt{2}\,v\end{aligned} \tag{B-26}$$

into Eqs (B-23) and (B-24) thus results in

$$\frac{d^2U}{du^2} + (2\nu + 1 - u^2)U = 0 \tag{63}$$

$$\frac{d^2V}{dv^2} + [-(2\nu+1) - v^2]V = 0 \tag{64}$$

Criteria Choice of N_{max}

The purpose of this section is to justify the choice made for N_{max} in Eq (75).

By examining Bessel function tables, it is seen that the leading terms of an array of $J_{\nu+n}(x)$ $(0 \leq \nu < 1$; $n = 0,1,2,...)$ have an absolute value greater than 10^{-2}. It is also known that $J_{\nu+n}(x)$ is a decreasing function for $\nu + n > x$ (Ref 5:365, 368). Thus, by choosing to truncate Eq (45) where the larger ordered Bessel functions have an absolute value less than 10^{-10}, results in the truncated-off terms (summed together) being less than one percent of the leading terms.

APPENDIX C

Theory of Bessel Function Subroutine

The purpose of this Appendix is to briefly describe the theory behind the Bessel function subroutine used in this thesis.

The subroutine to calculate $J_{\nu+n}(x)$ where $0 \leq \nu < 1$ and $n = (0,1,2,\ldots)$ (ν, x real) is a UNIVAC routine (Ref 10). It is divided into three regions of the argument; (1) $x < 10$, (2) $10 \leq x \leq 50$, and (3) $x > 50$.

(1) $x < 10$ (Ref 11:102-108). For a function F that obeys

$$F_{-\nu-1}(x) + F_{\nu+1}(x) = \frac{2\nu}{x} F_{\nu}(x) \qquad \text{(C-1)}$$

then let

$$F_{\nu+n}(x) = \alpha J_{\nu+n}(x) + \beta N_{\nu+n}(x)$$

for $M \gg N$. Defining

$$F_{\nu+M+1}(x) = 0$$
$$F_{\nu+M}(x) = a \qquad \text{(a is any real constant)} \qquad \text{(C-2)}$$

it can be shown that for

$$n \leq N \longrightarrow F_{\nu+n}(x) \simeq \alpha J_{\nu+n}(x) \tag{C-3}$$

For $n >> \frac{x}{2}$ and using the addition theorem

$$\sum_{m=0}^{L/2} \phi_m F_{\nu+2m}(x) = \alpha$$

where

$$\phi_o = \left(\frac{2}{x}\right)^{\nu} \Gamma(1+\nu)$$

$$\phi_m = \frac{(\nu+2m)(\nu+m-1)}{m(\nu+2m-2)} \tag{C-4}$$

Substitution of Eq (C-2) into Eq (C-1) yields an array of F values from $F_\nu(x)$ to $F_{\nu+M+1}(x)$. It is desired to have $M >> \frac{x}{2}$ so Eq (C-1) can be used to recur backward without loss of accuracy. Then Eq (C-4) is used to find α , and α in Eq (C-3) yields $J_{\nu+n}(x)$. The accuracy will depend on how large M is chosen.

(2) $10 \leq x \leq 50$ (Ref 12:18-26). $J_\nu(x)$ can be described by

$$J_\nu(x) = \left(\frac{B_\nu(t)}{t}\right) \frac{\sqrt{2}t}{\pi} \cos \phi_\nu(t) \tag{C-5}$$

where $t = 1/x$ and

$$\frac{B_\nu(t)}{t} = 1 + a_2 t^2 + a_4 t^4 + a_6 t^6 + \ldots$$

$$t\left[\phi_\nu + (\nu + \tfrac{1}{2})\tfrac{\pi}{2}\right] = 1 + b_2 t^2 + b_4 t^4 + b_6 t^6 + \ldots \quad \text{(C-6)}$$

(the routine truncates at t^{10}). For $|\nu| \leq 1$, Eqs (C-5) and (C-6) yield eight figure accuracy in $J_\nu(x)$ for $x > 8$. Equation (C-6) is also most rapidly convergent for ν close to one-half (i.e., most accurate for $\nu \to \frac{1}{2}$ and least accurate for $\nu \to 0$ and $\nu \to 1$). Eq (C-3) is then used to recur down, thus producing an array of $F_{\nu+n}(x)$. Equation (C-3) is then used to find α from $J_\nu(x)$ substitution of α into the $F_{\nu+n}(x)$ array then produces a $J_{\nu+n}(x)$ array $(n = 0,1,2,\ldots,N)$.

(3) $x > 50$. The same method (phase-amplitude) is used for $x > 50$ as in $10 \leq x \leq 50$. However, since computer time and memory are limited (especially for students), it is somewhat more difficult to get $M >> x/2$ necessary for backward recursion. Hence, $J_\nu(x)$ and $J_{\nu+1}(x)$ calculated using Eqs (C-5) and (C-6) are used in Eq (C-1) to recur forward. This method gives poor accuracy for large orders because for $\mu >> x/2$, $J_\mu(x) \simeq (x/2)^\mu$.

Modifications. The range $x > 50$ proved to be unacceptable for producing accurate values of $J_{\nu+n}(x)$ for large n ($n > x$) . Therefore, it was decided to recur backward for the extended range $10 \leq x \leq 100$. This proved to be very successful. Another modification attempted involved calculating a_{12} and b_{12} in Eq (C-6). This had very little effect on improving the routine.

This Bessel function subroutine is available by contacting:

Major Glenn R. Doughty
Air Force Institute of Technology
Department of Physics
Wright-Patterson AFB OH 45433

APPENDIX D

Additional Numerical Results

This appendix provides space for additional figures not placed in the main text. The non-availability of Bessel function tables for large order and argument limited the ranges of argument and order that could be verified. For example, Reference 13 only provided tables for fractional orders limited to $\pm 1/2$, $\pm 1/3$, $\pm 2/3$, and $\pm 3/4$ and only for $N = 0$. Reference 14, on the other hand, was limited to $N \leq 135$ and argument < 100 , with fractional order equal to zero.

TABLE (IV-1b)

Bessel Function Subroutine Check
Against Published Standards for $J_{\nu+N}(k\rho)$

Range: $0.001 \leq k\rho \leq 100$

$N = (0,1,2,\ldots,100)$

$\nu = 0.0$

$k\rho$	N	$J_N(k\rho)$ Subroutine	$J_N(k\rho)$ Standard*	Relative Error
.001	0	.9999997500	.9999997500	0.0
	1	.0004999999	.0004999999	0.0
	2	.012499990(-5)	.012499990(-5)	0.0
	3	.0000020833(-5)	.0000020833(-5)	0.0
.01	0	.9999750002	.9999750002	0.0
	1	.0049999375	.0049999375	0.0
	2	.0000124999	.0000124999	0.0
	3	.0020833203(-5)	.0020833203(-5)	0.0
1.0	0	.7651976866	.7651976866	0.0
	5	.2497577302(-3)	.2497577302(-3)	0.0
	10	.2630615124(-9)	.2630615124(-9)	0.0
	20	.3873503009(-24)	.3873503009(-24)	0.0
5.0	0	-.1775967713	-.1775967713	0.0
	5	.2611405461	.2611405461	0.0
	10	.1467802647(-2)	.1467802647(-2)	0.0
	20	.2770330052(-10)	.2770330052(-10)	0.0
10	0	-.2459357645	-.2459357645	0.0
	10	.2074861066	.2074861066	0.0
	20	.1151336925(-4)	.1151336925(-4)	0.0
	30	.1551096078(-11)	.1551096078(-11)	0.0
50	0	.5581232812(-1)	.5581232767(-1)	8.06(-9)
	20	-.1167043523	-.1167043528	4.28(-9)
	50	.1214090214	.1214090219	4.12(-9)
	100	.1115927365(-20)	.1115927368(-20)	2.69(-9)
100	0	.1998585061(-1)	.1998585030(-1)	1.55(-8)
	20	.6221745833(-1)	.6221745850(-1)	2.73(-9)
	50	-.3869834004(-1)	-.3869833973(-1)	8.01(-9)
	100	.9636667398(-1)	.9636667330(-1)	7.06(-9)

* For $k\rho = 0.001$ and 0.01 (Ref 14); For all other $k\rho$ (Ref 5)

Note: The number in parenthesis is the power of 10 by which the preceding number must be multiplied.

TABLE (IV-1c)

Bessel Function Subroutine Check
Against Published Standards for $J_{\nu+N}(k\rho)$

Range: $0.001 \leq k\rho \leq 100$

$N = 0$

$\nu = 1/4$

$k\rho$	$J_{1/4}(k\rho)$ Subroutine	$J_{1/4}(k\rho)$ Standard*	Relative Error
.001	.1649761767	.1649762131	2.21(-7)
.005	.2466957406	.2466957951	2.21(-7)
0.01	.2933679292	.2933679941	2.21(-7)
0.05	.4384768320	.4384769287	2.21(-7)
0.1	.5206577608	.5206578756	2.21(-7)
0.5	.7416564065	.7416565702	2.21(-7)
1.0	.7522311674	.7522313333	2.21(-7)
5.0	-.2809720038	-.2809720658	2.21(-7)
10	-.2063937413	-.2063937869	2.21(-7)
20	.1782983389	.1782983385	2.24(-9)
30	-.1246044299	-.1246044300	8.03(-10)
40	.5491175188(-1)	.5491175240(-1)	9.47(-9)
50	.1410606328(-1)	.1410606269(-1)	4.18(-8)
60	-.6642673498(-1)	-.6642673439(-1)	8.88(-9)
70	.9125954031(-1)	.9125953997(-1)	3.73(-9)
80	-.8570889767(-1)	-.8570889765(-1)	2.33(-10)
90	.5511011408(-1)	.5511011439(-1)	4.72(-9)
100	-.1107092717(-1)	-.1107092760(-1)	3.88(-8)

* (Ref 13)

Note: The number in parenthesis is the power of 10 by which the preceding number must be multiplied.

TABLE (IV-2b)

Fresnel Sine Integral Check
of Subroutine Versus Published Standards

Range: $0.0014137 \leq k\rho \leq 100.53096$

$N = (1,3,5,\ldots,N_{max})$

$\nu = 1/2$

U	$k\rho = \frac{\pi}{2}U^2$	(U)-Subroutine (see Eq(76b))	(U) Standard*	Relative Error
.03	.0014137	.0000141	.0000141	0.0
.04	.0025133	.0000335	.0000335	0.0
.06	.0056549	.0001131	.0001131	0.0
.09	.0100531	.0002681	.0002681	0.0
0.1	.015709	.0005236	.0005236	0.0
0.2	.0628319	.0041871	.0041876	1.19(-4)
0.5	.3926991	.0647320	.0647324	6.18(-6)
1.0	1.5707963	.4382590	.4382591	2.28(-8)
1.5	3.5342917	.6975009	.6975050	5.88(-6)
2.0	6.2831853	.3434101	.3434157	1.62(-5)
2.5	9.817477	.6191806	.6191818	1.62(-6)
3.0	14.137167	.4963041	.4963130	1.79(-5)
3.5	19.242255	.4152469	.4152480	2.65(-6)
4.0	25.132741	.4205120	.4205158	9.04(-6)
4.5	31.808626	.4342700	.4342730	6.91(-6)
5.0	39.269908	.4991865	.4991914	5.82(-6)
6.0	56.548668	.4469581	.4469608	6.04(-6)
6.5	66.366145	.5453716	.5453764	8.80(-6)
7.0	76.96902	.4997014	.4997048	6.80(-6)
7.5	88.357293	.4606970	.4607012	9.12(-6)
8.0	100.53096	.4602057	.4602142	1.91(-5)

* (Ref 5)

Note: The number in parenthesis is the power of 10 by which the preceding number must be multiplied.

TABLE (IV-3)

Bessel Summation Check of Routine for Eq (77)

Range: $0.001 \leq k\rho \leq 100$

$N = (0,1,2,\ldots,N_{max})$

$\nu = 0$

$k\rho$	Bessel Sum $1 \simeq J_o(k\rho)+2\sum_{N=1}^{N_{max}} J_{2N}(k\rho)$	Relative Error
.001	.99999975	2.50(-10)
.002	1.00000000	0.0
.003	1.00000000	0.0
.004	1.00000000	0.0
.005	1.00000000	0.0
.006	1.00000000	0.0
.007	1.00000000	0.0
.008	1.00000000	0.0
.009	1.00000000	0.0
.01	1.00000000	0.0
.05	.99999997	3.00(-10)
0.1	1.00000000	0.0
0.5	1.00000000	0.0
1.0	1.00000000	0.0
5.0	1.00000000	0.0
10	1.00000000	0.0
20	1.00000000	0.0
30	1.00000001	1.00(-10)
40	1.00000000	0.0
50	1.00000000	0.0
60	1.00000000	0.0
70	1.00000000	0.0
80	1.00000000	0.0
90	1.00000000	0.0
100	1.00000000	0.0

Note: The number in parenthesis is the power of 10 by which the preceding number must be multiplied.

TABLE (IV-4c)

Half-Plane Check of Subroutine
Versus Born and Wolf's Solutions

Angle of Incidence: $\theta_i = 22.5^\circ$

Distance from Edge: $0.001 \leq k\rho \leq 100$

$k\rho$	$\vec{J}_s \cdot \vec{J}_s^*$ Subroutine	$\vec{J}_s \cdot \vec{J}_s^*$ Born and Wolf	Relative Error
.001	.4684029211(3)	.4684029950(3)	1.57(-7)
.002	.2403209447(3)	.2403209813(3)	1.52(-7)
.003	.1634162387(3)	.1634162633(3)	1.50(-7)
.004	.1246239813(3)	.1246239998(3)	1.49(-7)
.005	.1011752171(3)	.1011752320(3)	1.47(-7)
.006	.8544027553(2)	.8544028804(2)	1.46(-7)
.007	.7413464357(2)	.7413465434(2)	1.45(-7)
.008	.6560952897(2)	.6560953843(2)	1.44(-7)
.009	.5894561983(2)	.5894562825(2)	1.43(-7)
.01	.5358948389(2)	.5358949148(2)	1.42(-7)
.05	.1366385829(2)	.1366384225(2)	1.17(-6)
0.1	.8189107747(1)	.8189002466(1)	1.29(-5)
0.5	.3467604171(1)	.3467593408(1)	3.10(-6)
1.0	.2963554436(1)	.2963273169(1)	9.49(-5)
5.0	.3469644246(1)	.3469617950(1)	7.58(-6)
10	.3388221165(1)	.3388136336(1)	2.50(-5)
20	.3404785885(1)	.3404684726(1)	2.94(-5)
30	.3409823380(1)	.3409763835(1)	1.75(-5)
40	.3412019465(1)	.3411990066(1)	8.44(-6)
50	.3413174576(1)	.3413084812(1)	2.63(-5)
60	.3413853061(1)	.3413817358(1)	1.05(-5)
70	.3414279933(1)	.3414280489(1)	1.63(-7)
80	.3414559925(1)	.3414560236(1)	9.11(-8)
90	.3413747647(1)	.3414747812(1)	4.87(-8)
100	.3414873892(1)	.3414873964(1)	2.13(-8)

* Normalized for $\sqrt{\frac{\epsilon_o}{\mu_o}}\, E_o = 1.$

Note: The number in parenthesis is the power of 10 by which the preceding number must be multiplied.

TABLE (IV-4d)

Half-Plane Check of Subroutine
Versus Born and Wolf's Solutions

Angle of Incidence: $\theta_i = 67.5^\circ$

Distance from Edge: $0.001 \leq k\rho \leq 100$

$k\rho$	$\vec{J}_s \cdot \vec{J}_s^*$ Subroutine	$\vec{J}_s \cdot \vec{J}_s^*$ Born and Wolf	Relative Error
.001	.6259299676(3)	.6259300619(3)	1.51(-7)
.002	.3158128663(3)	.3158129157(3)	1.56(-7)
.003	.2120104401(3)	.2120104731(3)	1.56(-7)
.004	.1599423065(3)	.159942331(3)	1.55(-7)
.005	.1286161098(3)	.1286161297(3)	1.55(-7)
.006	.1076814883(3)	.1076815049(3)	1.54(-7)
.007	.9269540169(2)	.9269541590(2)	1.53(-7)
.008	.8143313033(2)	.8143314274(2)	1.52(-7)
.009	.7265710850(2)	.7265710602(2)	1.51(-7)
.01	.6562384447(2)	.6562385430(2)	1.50(-7)
.05	.1429570778(2)	.1429570995(2)	1.51(-6)
0.1	.7620296496(1)	.7620297497(1)	1.31(-7)
0.5	.1995471355(1)	.1995466379(1)	2.49(-6)
1.0	.1219722187(1)	.1219690885(1)	2.57(-5)
5.0	.5581411230	.5581361479	8.91(-6)
10	.5005723246	.5005719124	1.02(-6)
20	.5259130666	.5258607850	9.94(-5)
30	.5671748589	.5671596962	2.67(-5)
40	.5943320126	.5942380397	6.68(-6)
50	.6039451152	.6039073894	6.25(-5)
60	.6004248186	.6004162077	1.43(-5)
70	.5909307243	.5909287139	3.40(-6)
80	.5820611890	.5820490309	2.09(-5)
90	.5777673975	5.777645033	5.01(-6)
100	.5787210245	.5787067379	2.47(-5)

*Normalized for $\sqrt{\frac{\varepsilon_o}{\mu_o}}\, E_o = 1$.

Note: The number in parenthesis is the power of 10 by which the preceding number must be multiplied.

TABLE (IV-4e)

Half-Plane Check of Subroutine
Versus Born and Wolf's Solutions

Angle of Incidence: = 90

Distance from Edge: 0.001 k 100

$k\rho$	$\vec{J}_s \cdot \vec{J}_s^*$ Subroutine	$\vec{J}_s \cdot \vec{J}_s^*$ Born and Wolf	Relative Error
.001	.6366196711(3)	.6366197723(3)	1.59(-7)
.002	.3183098356(3)	.3183098861(3)	1.59(-7)
.003	.2122065570(3)	.2122065908(3)	1.59(-7)
.004	.1591549178(3)	.1591549431(3)	1.59(-7)
.005	.1273239342(3)	.1273239545(3)	1.59(-7)
.006	.1061032786(3)	.1061032954(3)	1.59(-7)
.007	.9094566739(2)	.9094568175(2)	1.59(-7)
.008	.7957745888(2)	.7957747153(2)	1.59(-7)
.009	.7073551900(2)	.7073553025(2)	1.59(-7)
.01	.6366196710(2)	.6366197722(2)	1.59(-7)
.05	.1273239342(2)	.1273239544(2)	1.59(-7)
0.1	.6366196711(1)	.6366197721(1)	1.62(-7)
0.5	.1273239338(1)	.1273239544(1)	1.57(-7)
1.0	.6366195720	.6366197718	1.61(-7)
5.0	.1273239336	.1273239542	1.57(-7)
10	.6366196710(-1)	.6366197709(-1)	1.69(-8)
20	.3183098905(-1)	.3183098851(-1)	5.47(-9)
30	.2122065911(-1)	.2122065899(-1)	1.57(-9)
40	.1591549421(-1)	.1591549423(-1)	1.27(-8)
50	.1273239554(-1)	.1273239538(-1)	7.04(-9)
60	.1061032940(-1)	.1061032948(-1)	2.27(-8)
70	.0904568326(-2)	.9094568120(-2)	1.48(-8)
80	.7957747219(-2)	.7857747102(-2)	1.47(-8)
90	.7073552970(-2)	.7073552977(-2)	9.42(-10)
100	.6366197815(-2)	.6366197677(-2)	2.17(-8)

* Normalized for $\sqrt{\frac{\epsilon_o}{\mu_o}}\, E_o = 1.$

Note: The number in parenthesis is the power of 10 by which the preceding number must be multiplied.

TABLE (IV-4f)

Half-Volume Check of Subroutine

Versus Eq (58)

Range of incidence angles: $0° \leq \theta_i \leq 90°$

Distance from Edge: $0.001 \leq k\rho \leq 100$

θ_i	$k\rho$ *	Subroutine Value	Eq (58)	Relative Error
0.0	0.001	3.999999000	4.0	2.5(-7)
22.5	0.001	3.414213208	3.414213562	1.04(-7)
45.0	0.001	2.000000499	2.0	2.5(-7)
67.5	0.001	0.5857867902	0.5857864376	6.0(-7)
90.0	80.0	6.757530467(-19)	0.0	6.76(-19)

* Value of $k\rho$ where the maximum relative error occurs.

Relative error here is defined simply as the difference between the Subroutine and Eq (58) because one cannot divide by zero.

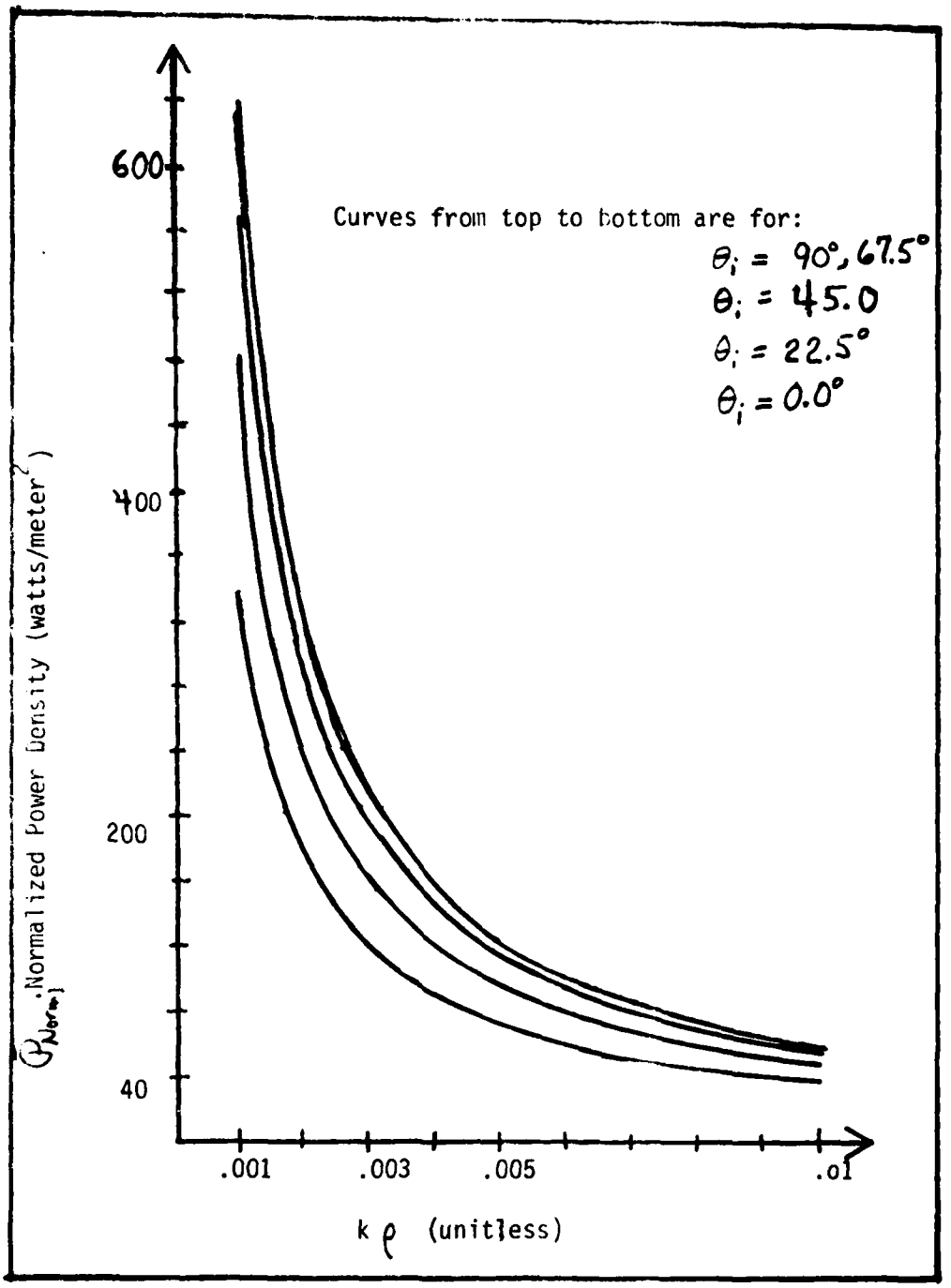

Figure 24. Normalized Power Density Vs. k ,TM Half-plane

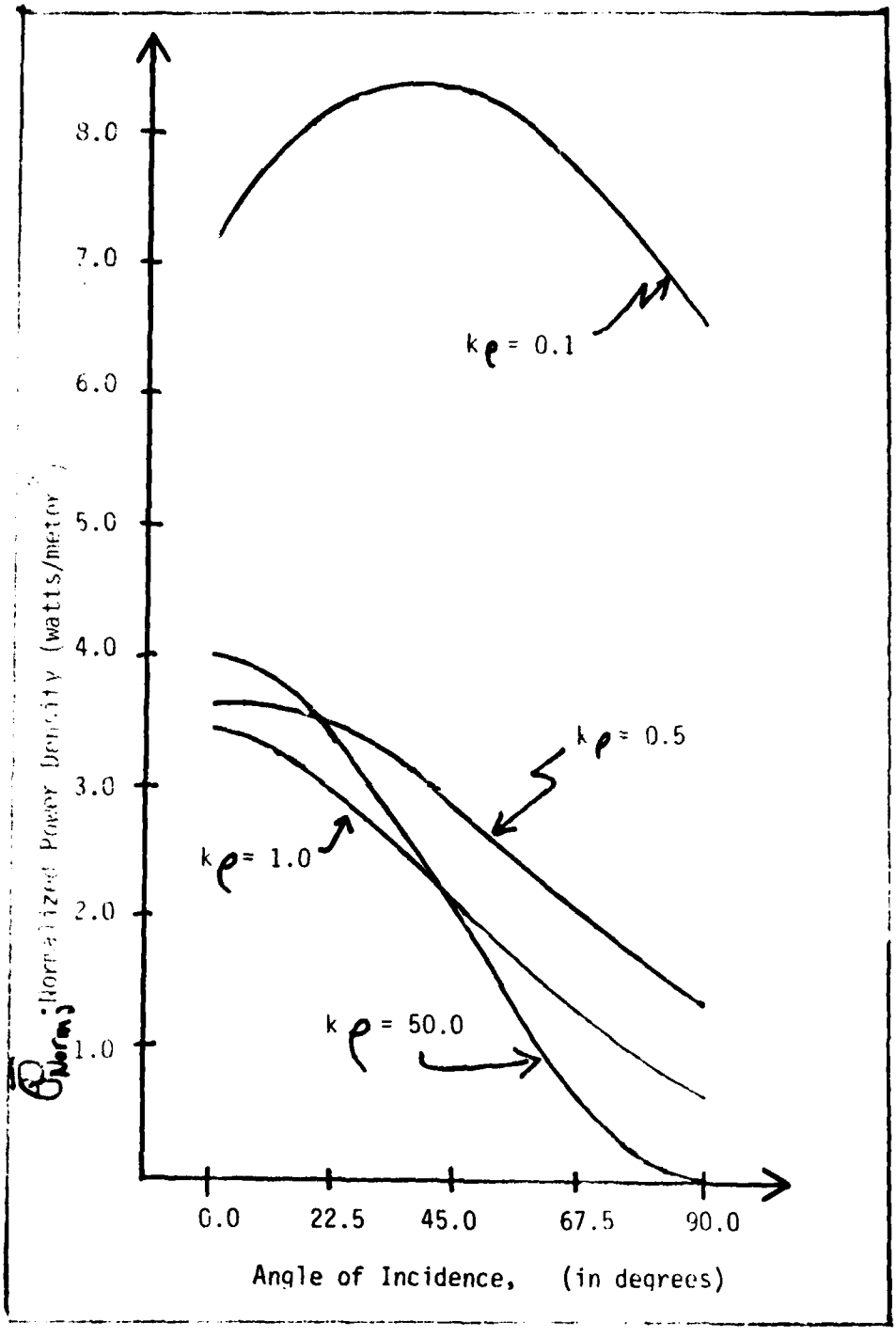

Figure 25. Normalized Power Density Vs. θ_i, TM Half-plane

Vita

James F. Berke was born on 10 December 1954 in Chicago, Illinois. He graduated from Homewood-Flossmoor High School in Chicago in 1972. After attending the University of Chicago for 1-1/4 years, he enlisted in the United States Air Force. In 1976 he was released from active duty to enter the Air Force ROTC at Illinois Institute of Technology. He graduated with a B.S.E.E. from IIT in 1979. He entered the Air Force Institute of Technology in June 1979 to obtain a Master of Science degree in Electro-Optics.

Permanent Address: 950 Coach Road
Homewood, Illinois 60430

UNCLASSIFIED

SECURITY CLASSIFICATION OF THIS PAGE (When Data Entered)

REPORT DOCUMENTATION PAGE	READ INSTRUCTIONS BEFORE COMPLETING FORM
1. REPORT NUMBER: AFIT/GEO/PH/80-3	2. GOVT ACCESSION NO.: AD A094401
	3. RECIPIENT'S CATALOG NUMBER:
4. TITLE (and Subtitle): INVESTIGATION OF LASER HEATING IN COMPONENTS WITH SHARP EDGES	5. TYPE OF REPORT & PERIOD COVERED: MS Thesis
	6. PERFORMING ORG. REPORT NUMBER:
7. AUTHOR(s): JAMES F. BERKE, 2LT, USAF	8. CONTRACT OR GRANT NUMBER(s): Master's Thesis
9. PERFORMING ORGANIZATION NAME AND ADDRESS: Air Force Institute of Technology (AFIT-EN) Wright-Patterson Air Force Base, Ohio	10. PROGRAM ELEMENT, PROJECT, TASK AREA & WORK UNIT NUMBERS:
11. CONTROLLING OFFICE NAME AND ADDRESS:	12. REPORT DATE: December 1980
	13. NUMBER OF PAGES: 127
14. MONITORING AGENCY NAME & ADDRESS (if different from Controlling Office): 127	15. SECURITY CLASS. (of this report): UNCLASSIFIED
	15a. DECLASSIFICATION/DOWNGRADING SCHEDULE:

16. DISTRIBUTION STATEMENT (of this Report)

Approved for public release; distribution unlimited.

17. DISTRIBUTION STATEMENT (of the abstract entered in Block 20, if different from Report)

18. SUPPLEMENTARY NOTES: Approved for public release; IAW AFR 190-17

06 JAN 1981

FREDERICK C. LYNCH, Major, USAF
Director of Public Affairs

19. KEY WORDS (Continue on reverse side if necessary and identify by block number)

Laser Heating

Fractional Order Bessel Functions

Sharp Edge Effects

20. ABSTRACT (Continue on reverse side if necessary and identify by block number)

Numerical results are presented for the approximate time-averaged power density dissipated on the surface of a highly conductive infinite wedge (of angle 90°) near the vicinity of the sharp edge. The numerical results are normalized so one may readily obtain results for varying incident wave frequencies. The angle of incidence of the incident radiation, θ_i, (measured with respect.

(Continued on reverse)

DD FORM 1 JAN 73 1473 EDITION OF 1 NOV 65 IS OBSOLETE

UNCLASSIFIED

SECURITY CLASSIFICATION OF THIS PAGE (When Data Entered)

Thesis

012225

BLOCK 20: Abstract (Cont'd)

to the surface normal of the wedge), is varied from $\theta_t = 0°$ (normal incidence) to $\theta_t = 90°$ (grazing incidence). In particular, numerical results for TE and TM polarization are presented for incident wavelengths of 3.8 mm and 10.6 (μm). It is assumed that the power density absorbed (watts/m^2) is all converted to heat density.

To accept the validity of the results, an extensive check is made on an arbitrary (real) order Bessel function subroutine used in the equation necessary for the numerical calculations. General electromagnetic theory is also discussed and extended to the use in specific geometries. The geometries considered besides the wedge (though with no numerical results) are the parabolic cylinder and infinite cone.

In conclusion, the numerical results seem very promising due to the success of verifying the Bessel function subroutine used in the calculations.